Nonequilibrium Bose condensation in a pumped dye-filled photonic cavity

vorgelegt von
M. Sc.
Martina Vlaho
ORCID: 0000-0002-1214-6790

an der Fakultät II – Mathematik und Naturwissenschaften
der Technischen Universität Berlin
zur Erlangung des akademischen Grades

Doctor rerum naturalium
- Dr. rer. nat.-

genehmigte Dissertation

Promotionsausschuss:

Vorsitzender: Prof. Dr. Markus R. Wagner
Gutachter: Prof. Dr. André Eckardt
Gutachter: Prof. Dr. Jonas Ola Oscar Larson

Tag der wissenschaftlichen Aussprache: 22. April 2022

Berlin 2022

Declaration of Authorship

I declare that this thesis is my own work and has not been submitted to this or any other academic institution for any other degree or qualification.

Chapters 4 through 6 are adapted from my published papers (referenced in the chapters) and all the writing, calculations and figure production was done by me.

I declare that I have acknowledged all main sources of help and appropriately referenced the published work of others.

TECHNISCHE UNIVERSITÄT BERLIN

Abstract

Faculty II - Mathematics and Natural Sciences

Institute for Theoretical Physics

Nonequilibrium Bose condensation in a pumped dye-filled photonic cavity

by Martina Vlaho

An effectively two-dimensional photon gas trapped in a dye-filled microcavity can undergo thermalization and equilibrium-like Bose-Einstein condensation. However, given the inherently driven-dissipative nature of this system, it can exhibit a complex interplay between the thermalizing influence of the environment given by the dye solution and the pump and loss processes driving the system out of equilibrium. We first consider a homogeneously pumped photon gas and investigate how its steady state is affected when varying the pump power, the cavity lifetime and the cutoff frequency. Depending on the parameter regime, the selection of modes that acquire large occupation can be related either to lasing of (typically multiple) modes or to a quasiequilibrium condensation in the ground state. We calculate and explain the phase diagram of the system, with a particular emphasis on the role played by mode competition that occurs in the regime of weak cavity loss. We then consider the case where the system is driven asymmetrically (by a relatively narrow off-centered pump beam) and find that it features a robust and controllable mechanism for two-mode emission. Namely, after the system starts lasing in the dominantly pumped excited mode, in a second transition a photon condensate is formed in the ground mode, when the pump power is increased further. This effect is a consequence of the redistribution of excited dye molecules via the lasing mode in combination with thermalization. We demonstrate how this effect can be controlled further by tailoring the effective transverse potential for the photons. This allows for the threshold pump power to be tuned by orders of magnitude. For this scenario we formulate a simplified, analytically solvable model which gives a very good agreement, both qualitative and quantitative, with the full original model.

Acknowledgements

I would first like to thank my supervisor, Prof. Dr. André Eckardt for his continuous guidance and support throughout the entire duration of my doctoral studies.

I would also like to thank H.A.M. (Alex) Leymann and Daniel Vorberg for their contributions and very helpful discussions in the first period of my doctoral project.

Finally, I want to express my gratitude to my family, especially my parents, for their unconditional support and patience.

Contents

Abstract **v**

Acknowledgements **vii**

1 Introduction **1**

2 Review **5**
  2.1 Lasing 5
  2.2 Bose-Einstein condensation of ideal bosonic gas 7
  2.3 Properties of equilibrium-like photon condensate 10
    2.3.1 Chemical potential of light and Kennard-Stepanov law 10
    2.3.2 Grand-canonical number fluctuations in photon BEC 14

3 System and model **17**
  3.1 Master equation 20
  3.2 Derivation of the rate equations from the master equation 22
  3.3 Phenomenological quasi-derivation of the rate equations 26
  3.4 Mode selection 28
  3.5 Equilibrium limit 29

4 Homogeneously pumped photon gas **31**
  4.1 Threshold pump rate 32
  4.2 Tuning the photon cavity lifetime and mode competition 34
  4.3 Phase diagram 39
  4.4 Tuning the cutoff frequency 40

5 Off-centered pump beam **45**
  5.1 Non-equilibrium steady state and lasing assisted ground-state condensate . 47

6 Structured cavity **51**
  6.1 Controlled two-mode emission 51
  6.2 Effect of inter-well resonance 54

7 Simplified model and analytic solutions **55**

8 Conclusions 65

A Full analytic solution of a simplified model 67

Bibliography 71

List of Figures

2.1 Basic components of a laser 6

2.2 Number of laser photons n (solid blue line) and number of excited atoms N (dashed orange line) vs pump rate P. 7

2.3 Condensate fraction as a function of temperature for a 2D harmonic (solid blue line) and a 3D box potential (dashed orange line). 9

2.4 Upper panel: absorption and fluorescence spectra of a dye solution. Lower panel: photochemical reaction between the photons, the ground-state and the excited-state molecules. The molecule in the ground-state becomes excited by absorbing a photon of frequency ω. The two electronic states of the dye molecule have an additional structure, labeled $S_\downarrow$ and $S_\uparrow$, corresponding to rovibrational states. The frequency of the bare electronic transition (zero-phonon line) is denoted by ω_{zpl}. 12

3.1 Schematically illustrated experimental setup containing an optical microresonator filled with a dye solution and pumped with an external laser. 17

3.2 Left panel: spherically curved mirrors (with radius of curvature R) separated by $D(r)$, which depends on the distance r from the optical axis. Right panel: reshaping of the mirrors produces a different potential. The requirement that the boundary conditions imposed by the cavity are locally satisfied, results in a variation of the optical wavelength, and correspondingly, the effective potential experienced by the photons. 19

3.3 Photon mode densities $|\psi_{n_x,n_y}(x)|^2$ projected onto the x axis. For simplicity, only modes $(n_x, 0)$, with nodes only along x direction, are shown. . . . 20

3.4 Illustration of the model showing all of the processes contained in the dissipative part of the Lindblad master equation. 21

4.1 Fitted absorption and emission rates (solid lines) vs. frequency ε_i/h. The rates are fitted to experimental data (crosses) [19, 49] using a cubic smoothing spline. The frequency range of the relevant cavity modes is indicated by the shaded gray area with a sharp cutoff at $\omega_c = \varepsilon_0/\hbar$. 32

4.2 Threshold pump rate P_{th} of the first selection as a function of the thermalization parameter ξ and the energy E_i of the modes. 33

4.3 The left panel shows the mode populations n_i as functions of pump rate P for two values of the thermalization parameter, $\xi = 0.03$ (a) and $\xi = 20.1$ (c). Only one of the modes in an almost identically behaving symmetric pair is labeled. The right panel, (b) and (d), shows the corresponding spatial distributions of excited dye molecules $f(x)$ for the chosen values of P (vertical lines in the left panel). 34
4.4 Spatial distributions of excited dye molecules $f(x)$ close above the first selection threshold P^{th} for 4 values of the thermalization parameter ξ. The corresponding threshold gain G^{th} is marked by a horizontal blue line of the same style. 35
4.5 Population n_i (a) and gain G_i (c) of modes i vs. pump rate P for $\xi = 1.8$. Only one of the modes in an almost identically behaving symmetric pair is labeled. Dotted horizontal lines indicate threshold values G_i^{th} to which the gain is clamped at selection. The middle panel (b) shows the zoomed-in gain of modes (2,0) and (0,2), which are deselected when the clamped gain starts to drop below $G^{th}_{(2,0)}$ and $G^{th}_{(0,2)}$, respectively. 36
4.6 Phase diagram showing three main regions. The white region has no selected modes, only the ground mode is selected in the blue region, and there are multiple selections in the gray one. Colored dots (crosses) are numerical points indicating selections (deselections) of the corresponding modes. The dotted line is the lower (upper) phase boundary, interpolating between the points of first (second) selection. The pump rate at which the two phase boundaries meet is the minimal P for which the ground mode is selected. Below this pump rate (“lasing phase"), the phase boundaries are indistinguishable, because multiple quasi-degenerate higher energy modes are selected at almost exactly the same P. The analytical result for the first selection threshold (Eq. (4.3)), is shown with a solid black line. In the high ξ regime, this phase boundary approaches the dashed horizontal line, showing the high thermalization limit of Eq. (4.3) $P^{th}(\xi \to \infty)$. The three dotted vertical lines mark the cuts through the phase diagram shown in Fig 4.3 and Fig 4.5. 38
4.7 Numerical mode population n_i (blue dots) vs mode energy E_i compared to the thermal distribution (orange straight line) below, close above and far above the first selection threshold P^{th} when $\xi = 1 \Rightarrow P^{th} = 0.0065\,\Gamma$ (left panels) and $\xi = 100 \Rightarrow P^{th} = 0.0044\,\Gamma$ (right panels). 40
4.8 Population n_i of modes i vs. pump rate P for $\xi = 1$. The cutoff frequency is $\omega_c/2\pi = 490$ THz (a), $\omega_c/2\pi = 515$ THz (b) and $\omega_c/2\pi = 525$ THz (c). The inset of panel (c) contains the same result extended to high P regime, showing that only the ground mode is selected before the gain is saturated. 41

4.9 The upper panels correspond to the case of a wide Gaussian pump profile and show the mode populations n_i vs. P (a) and $f(x)$ for the chosen values of P (b), indicated by the vertical lines in the left panel. The same quantities are shown in the lower panels (c, d) for the case of a constant pump profile. In both cases the thermalization parameter is $\xi = 4$. 42

5.1 Off-centered Gaussian pump spot (P) and photon modes $|\psi_{n_x,n_y}(x)|^2$ projected onto the x axis. For simplicity, only modes $(n_x, 0)$, with nodes only along x direction, are shown. 46

5.2 Population n_i of mode i vs. pump rate P for $\xi = 0.04$ (a) and $\xi = 6$ (c). Spatial distributions $f(x)$ of excited dye molecules along the x-axis (b, d) is shown for $\xi = 0.04, 6$ at those P marked by the corresponding vertical lines in (a, c), respectively. The shaded area represents $p(x)/\Gamma$. The threshold gain of the ground mode G_0^{th} is indicated by the dashed blue line. 46

5.3 Threshold pump rate P_i^{th} for the first selection [Eq. (5.1)] vs. pump-spot position μ for $\xi = 6$. The different colors and labels (n_x, n_y), separated by dotted vertical lines, indicate which mode is selected. The dots are obtained numerically form the full rate equations. The colored bars at the bottom indicate the mode with the largest overlap with the pump profile $G_i[g_{\mu,\sigma}(\vec{r})]$ and the arrow points to the case shown in Fig. 5.2(c, d) 48

5.4 Population n_i of mode i vs. pump rate P for $\xi = 2,\ \mu/d = 3.2$ (a), $\xi = 3,\ \mu/d = 3.25$ (b) and $\xi = 4,\ \mu/d = 3.1$ (c). In each case, the threshold pump rate for the ground mode is marked by the dotted gray line. 49

5.5 Population n_i of mode i vs. pump rate P (a) for $\xi = 15,\ \mu/d = 3.2$. Spatial distribution $f(x)$ of excited dye molecules along the x-axis (b) at those P marked by the corresponding vertical lines of the same style in (a). The shaded area represents $p(x)/\Gamma$. The threshold gain of the ground mode G_0^{th} is indicated by the dashed blue line. 50

6.1 Upper panel: Double well potential and modes $|\psi_i(x)|^2$ for $\delta = 0.79\ d$ together with the pump spot (P), projected onto the x-axis. The modes shown in color (blue and purple) and labeled by their energy are those that get selected. Lower panel: For a slightly different value $\delta = 0.81\ d$, the lasing mode 6 becomes delocalized between both wells, as a consequence of an inter-well resonance. 52

6.2 Mechanism for creating a variable potential landscape for photons trapped in a microcavity [30] 53

6.3 Mode populations n_i vs pump rate P for two slightly different values of δ. The grey area indicates a P range in which there is only lasing, while in the blue region the ground-state condensate is also present. 53

6.4 Phase diagram showing the resonance effect on the ground-state condensate. The two phase boundaries are numerically obtained threshold pump rates P^{th} for the lasing (gray) and the ground-state condensation (blue) as functions of δ. The arrows in the inset (zoom-in) correspond to the case shown in Figs. 6.1 and 6.3. 54

7.1 Simplified model: two modes, labeled E_0 and E_e are taken into account, as well as a spatially constant fraction of excited molecules in two regions separated by a plane (dashed line passing through the barrier center x_B), such that the ground mode can be taken as completely localized in the left one, whereas the excited mode can be distributed between both wells, with the respective fractions labeled by α_1 and α_2. Only the upper well is pumped with a constant rate P. 55

7.2 Lower panel: analytically obtained mode populations $n_{0,e}$ vs P for $\xi = 1$ and $\delta/d = 0.46$, for which the excited modes (E_3) is selected first, followed by the ground-mode selection. The two threshold values of P, indicated by dotted vertical lines, separate three regimes (pump-rate intervals), labeled 1, 2 and 3. They correspond to the three qualitatively different solutions of the system of equations (7.3). Upper panel: the double-well potential for this value of δ with the two selected modes shown in color. 57

7.3 Mode populations $n_{0,e}$ vs P for $\xi = 1$ and 4 values of the parameter δ, for which various excited modes (E_e) shown in different colors are selected first, followed by the ground-mode selection (blue) in each case. Results obtained analytically using the simplified model are shown as dashed lines with the corresponding threshold P values marked by dotted vertical lines, whereas the numerical solutions of the original rate equations [(3.15), (3.16)] are shown as solid lines. 59

7.4 Threshold pump rate P^{th} vs ξ for the first selection of mode e (purple) and the second one of the ground mode (blue), for $\delta/d = 0.79$ (a) and $\delta/d = 0.81$ (b). The analytically obtained results (solid curves) are compared with the numerical ones (dots interpolated by dotted lines to guide the eye). . . 60

7.5 Top panel: threshold pump rate P^{th} vs δ for the first selection of the excited mode (gray) and the second one of the ground mode (blue). The analytically obtained results $P^{th,0(e)}_{model}$ (solid curves) are compared with the numerical ones, $P^{th,0(e)}_{num}$ (dots). The three qualitatively different regimes are shown with different colors, white (no modes selected), gray (only mode e selected) and blue (ground mode also selected). The two resonance points marked by arrows are shown magnified in the two lower panels. 62

7.6 Simplified model applied to the case of asymmetrically pumped harmonic trap. The border between 2 spatial regions is placed between the ground mode and the pump, where they both become vanishingly small. 63

7.7 Mode populations $n_{(0,0)}$ and $n_{(e,0)}$ vs P for $\xi = 6$ (a) and $\xi = 0.04$ (b). Results obtained analytically using the simplified model are shown as dashed lines with the corresponding threshold P values marked by dotted vertical lines, whereas the numerical solutions of the original rate equations [(3.15), (3.16)] are shown as solid lines. 63

A.1 Lower panel: analytically obtained mode populations $n_{0,e}$ vs P for $\xi = 1$ and $\delta/d = 0.46$, for which the excited modes (E_3) is selected first, followed by the ground-mode selection. The corresponding threshold values of P, indicated by dotted vertical lines, separate the three solutions of the system of equations (7.3). Upper panel: the double-well potential for this value of δ with the two selected modes shown in color. 68

Chapter 1

Introduction

Following the first experimental realization of Bose-Einstein condensation (BEC) in very dilute atomic gases [1, 2], BEC of quasiparticles, like exciton-polaritons has also been observed [3–8], which lead to the question of whether photons themselves can undergo a similar quasiequilibrium transition.

Photons harmonically trapped in a dye-filled microcavity with appropriate characteristics can be described as a 2-dimensional gas of bosons with a nonzero effective mass. This system can be used as a platform for studying the interplay between driving and loss on the one hand and thermalization (via the rovibrational relaxation of the dye molecules interacting with the environment given by the solvent) on the other. While the former process describes lasing [9], about a decade ago the regime where thermalization is the dominant process, has been realized and equilibrium-like Bose condensation of photons was observed in various systems [10–17].

Unlike the Bose-Einstein condensate of an atomic gas, which was realized at a very low critical temperature and in a microcanonical setup, a quasiequilibrium photon condensate, forms at room temperature (above a critical photon number) and under grand-canonical conditions. This inherently grand-canonical statistics of photon BECs [18] has been studied, as well as its spatial [19] and temporal features [20–23]. A considerable amount of work has also been done to clarify the delimitation of photon BECs from lasers [24–28]. Other research in this area includes the investigation of thermo-optic interaction effects [29] and the use of thermo-optic imprinting to create variable potentials for coupled photon condensates [30].

Given the inherently driven-dissipative nature of these systems, a complex interplay between the pump and loss processes driving the system out of equilibrium and the thermalizing influence of the environment (dye solution), emerges when tuning the various control parameters. This non-equilibrium nature of these systems makes them an excellent experimental platform for studying ordering under non-equilibrium conditions. The case of a symmetrically pumped system and its steady-state featuring multi-mode condensates has been studied experimentally [16], as well as theoretically [31]. It was found that excited cavity modes start to emit coherently together with the ground mode, when the pump power and the photon loss are increased relative to the thermalizing coupling to the dye. A complex network of different phases in parameter space is predicted, each of which is characterized by different combinations of macroscopically populated modes [31].

Part of this thesis is also concerned with the case of a symmetrically (homogeneously) pumped system, in which multi-mode condensates occur. We show how the limit of quasi-equilibrium photon BEC is approached via mode competition when the photon cavity lifetime is increased. Moreover, we also discuss the role played by the cutoff frequency, i.e. the ground-mode energy, in the formation of multi-mode condensates [32].

We then turn our attention to a nonequilibrium scenario, where the system is driven by an off-centered pump beam. This scenario is shown to feature a robust mechanism for controlled two-mode emission [33]. We find that the system undergoes two pump-power driven nonequilibrium phase transitions. First, the system starts to lase in an excited mode, which is directly determined by the position of the pump spot. When the pump power is increased further, the spatial redistribution of pump power mediated by this lasing mode then triggers a second transition, where thermalization leads to the additional formation of a macroscopically occupied ground mode.

We then exploit this effect for engineering controlled and robust two-mode emission by tailoring the transverse potential landscape for the photons. Specifically, we choose an asymmetric double-well potential and show that when pumping its upper minimum, the second transition threshold can be shifted by orders of magnitude by tuning the system close to or further away from interwell resonances. We also formulate a simplified, analytically solvable model, which reproduces the qualitative features of the numerical results and also agrees with them quantitatively to a high degree.

This thesis is organized as follows. In chapter 2, we present a review of several topics which are very relevant for the discussion following in the main part of this manuscript. In chapter 3 we introduce the model system, described in terms of a Lindblad master equation, from which the rate equations for the photon mode populations n_i, and the spatially dependent fraction $f(\vec{r})$ of excited dye molecules are derived. We then discuss the condition for mode selection, i.e. a mode acquiring macroscopic occupation, before ending this chapter by explaining how this condition is connected to the locking of the chemical potential as a BEC condition in the equilibrium limit.

In chapter 4 we discuss the numerical results for the case of a homogeneously pumped photon gas. First we list all the parameter values corresponding to the relevant experiments and used in the numerical simulations. Then we present a general condition for the threshold pump rate for a mode selection, which reduces to very simple expression in the case of first selection. In the next section, we investigate the dependence of mode selection on the so-called thermalization parameter, which is effectively a dimensionless photon cavity lifetime. Here we observe and discuss the effects of mode competition and deselection (loss of macroscopic occupation) [31], before presenting a phase diagram in a parameter plane spanned by the pump rate and the thermalization parameter. We explain the various phase boundaries and how the approach towards a quasi-equilibrium ground-mode condensate manifests in the phase diagram. Moreover, we point out discrepancies with respect to the previously computed phase diagram of Ref. [31]. In the final section of this chapter we study how the mode selection is affected when tuning the cutoff-frequency.

The case of asymmetrically pumped system is investigated in chapter 5. Here we observe the effect of lasing-assisted ground-mode condensation. This two-mode emission is explored further in chapter 6, where the harmonic trap is replaced with an asymmetric double-well potential. We find that interwell resonances can be used to tune the threshold for the ground-mode condensation over a wide range of pump power.

In chapter 7 we present a simplified model for the case discussed in the previous chapter and which is solved analytically. It reproduces the qualitative features of the numerically obtained solutions of the original model, and the quantitative agreement between the two models is also very good. The full analytic solution of the toy model is given in appendix A.

Chapter 2

Review

The purpose of this chapter is to present a condensed recapitulation of several topics which are important for the discussion following in the main part of this manuscript. We start with a brief description of lasing and continue to review the phenomenon of Bose-Einstein condensation in the next section. Finally, some key properties of the equilibrium-like photon condensate, first observed in Ref. [11], are discussed and derived.

2.1 Lasing

In contrast to other light sources, laser light is characterized by a high degree of both spatial and temporal coherence. Lasers can be categorized by the type of active ("gain") medium. This is a material which is brought into an excited state and used to amplify light through a process of stimulated emission, in which the output photons have the same direction, wavelength and polarization as the stimulating ones. The main components of a laser system are shown in Figure 2.1. Typically, the gain medium is placed in an optical resonator with mirrors on each side. One of the them is partially transparent allowing some of the light to escape (and form the laser beam). The emitted light is reflected inside the resonator so that it can pass through the gain medium repeatedly and get amplified via stimulated emission. Although the active medium amplifies any photons passing through it, irrespective of their direction, only photons in a spatial mode supported by the resonator will pass through it more than once and obtain significant amplification. The gain medium must also be "pumped" (supplied with energy by an external source) in order for its constituent particles to be predominantly in an excited state (population inversion). The rate of stimulated emission then exceeds the absorption rate. Usually, an electric current (semiconductor lasers) or light at a different wavelength (solid-state lasers) is used as the energy source. In a continuously pumped laser the processes leading to light amplification are balanced by the loss mechanisms (e.g., through mirror transmission) and a steady state (fixed point) can be achieved, where lasing appears above some minimal value of the

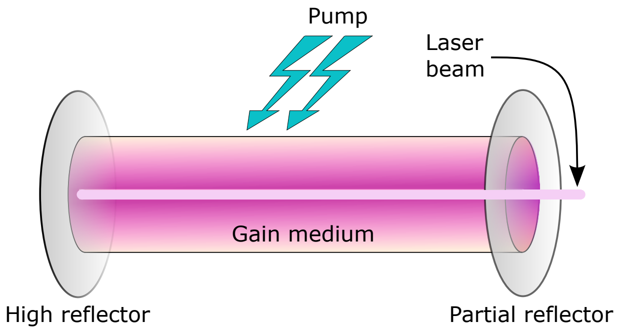

FIGURE 2.1: Basic components of a laser

pump power, called the lasing threshold [9]. Below this value of the pump power, the lasing mode (i.e., the cavity mode undergoing the lasing transition) is negligibly populated, as are all the other modes. Above it, there is a macroscopic occupation in the lasing mode.

One of the simplest phenomenological models of laser dynamics is given by the following system of coupled nonlinear differential equations for the number of excited atoms (or molecules) N of the gain medium and the number of photons n in the lasing mode [34]

$$\begin{aligned} \dot{n} &= gnN - \kappa n \\ \dot{N} &= P - \Gamma N - gnN \end{aligned} \tag{2.1}$$

Here, g is the gain coefficient of stimulated emission (relative to absorption), κ is photon loss rate (e.g., through mirror transmission) and P is the pump rate. The gain term gnN is proportional to n due to stimulated emission of the lasing mode, while the spontaneous emission into this mode is neglected. The decay rate of spontaneous emission into other (non-lasing) modes is given by Γ.

Solving for the steady state leads to two qualitatively different regimes. Below the lasing threshold given by

$$P_{th} = \kappa\Gamma/g, \tag{2.2}$$

the number of laser photons remains zero in the approximation where spontaneous emission is neglected, while the number of excited atoms increases linearly with the pump rate $N = P/\Gamma$. Above the lasing threshold N remains fixed at value $N_{th} = \kappa/g$, because any "surplus" of excited atoms is converted into laser photons (so-called clamping of the gain). That is, P_{th} marks the onset of lasing and the number of laser photons is given by

$$n = \frac{P}{\kappa} - \frac{\Gamma}{g} \ , \quad P > P_{th}. \tag{2.3}$$

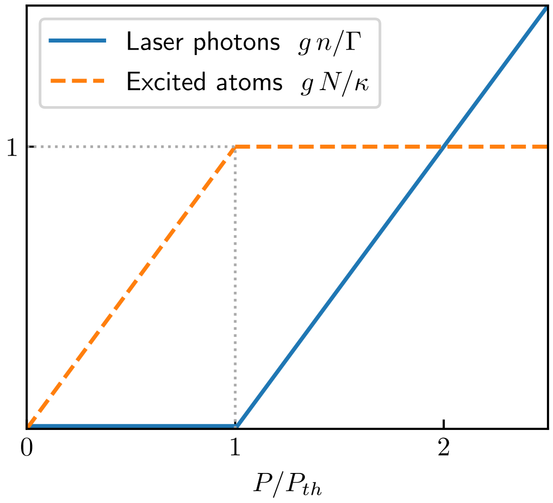

FIGURE 2.2: Number of laser photons n (solid blue line) and number of excited atoms N (dashed orange line) vs pump rate P.

In figure 2.2 the number of laser photons n (solid blue line) and the number of excited atoms N (dashed orange line) are shown as a function of pump rate P.

2.2 Bose-Einstein condensation of ideal bosonic gas

A system of non-interacting bosons will be distributed into the energy eigenstates according to the Bose-Einstein distribution. That is, the average number of bosons occupying a state i is given by

$$n_i = \frac{1}{e^{\beta(\varepsilon_i - \mu)} - 1}, \tag{2.4}$$

where β is the inverse temperature $1/k_BT$, μ is the chemical potential and ε_i the energy of state i. Given that $n_i > 0 \ \ \forall i$, it follows that the chemical potential must be $\mu \leq \varepsilon_0$ and in particular, $\mu \to \varepsilon_0$ (the so-called locking of the chemical potential) corresponds to a divergent occupation in the ground mode. For simplicity, we can choose the lowest energy to be zero, $\varepsilon_0 = 0$.

The total number N of bosons is

$$N = \sum_i n_i \cong \int_0^\infty g(\varepsilon) n(\varepsilon) d\varepsilon, \tag{2.5}$$

where $g(\varepsilon)$ is the density of states. This approximation, where the entire sum over states is replaced with an integral, implies an infinitesimally small contribution of each value ε to the total particle number, including $\varepsilon = 0$, corresponding to the ground state. This is no longer valid at low temperatures, at which bosons start to increasingly accumulate in the ground state. Therefore, this contribution of the lowest state must be separated from the integral and we get [35]

$$N = n_0 + N' = \frac{z}{1-z} + \int_0^\infty \frac{g(\varepsilon)d\varepsilon}{e^{\beta\varepsilon}/z - 1}, \tag{2.6}$$

where $n_0 = z/(1-z)$ is the number of bosons in the ground state and the so-called fugacity $z = e^{\beta\mu}$ is introduced for convenience.

If we insert the density of states for massive free particles in 3-dimensional (3D) space [1], $g(\varepsilon) \sim \sqrt{\varepsilon}$, expand the integrand and integrate term by term, we finally get

$$N = \frac{z}{1-z} + \frac{V}{\lambda^3} F(z), \tag{2.7}$$

where $\lambda = h/\sqrt{2\pi m k_B T}$ is the thermal de Broglie wavelength of particles with mass m at temperature T and a function of fugacity

$$F(z) = \sum_{m=1}^{\infty} \frac{z^m}{m^{3/2}} \tag{2.8}$$

has been introduced. When $z \to 1$, the number of particles outside the ground mode N' is at most

$$N' = \frac{V}{\lambda^3} F(1) = \frac{V}{\lambda^3} \zeta(3/2) \approx 2.612 \frac{V}{\lambda^3}, \tag{2.9}$$

where ζ is the Riemann zeta function. We now define a temperature T_c such that

$$N = 2.612 \frac{V}{\lambda_c^3}, \tag{2.10}$$

where λ_c is the thermal de Broglie wavelength at temperature T_c. Then the number of particles in the ground mode is

$$n_0 = N - N' \approx N \left[1 - \left(\frac{T}{T_c} \right)^{3/2} \right]. \tag{2.11}$$

Therefore, if T is even slightly below the critical temperature T_c, a significant fraction of the total number of bosons will be in the lowest state, whereas for temperatures above T_c,

---

[1] The density of states is obtained via the usual “particle in a box” treatment for free particles.

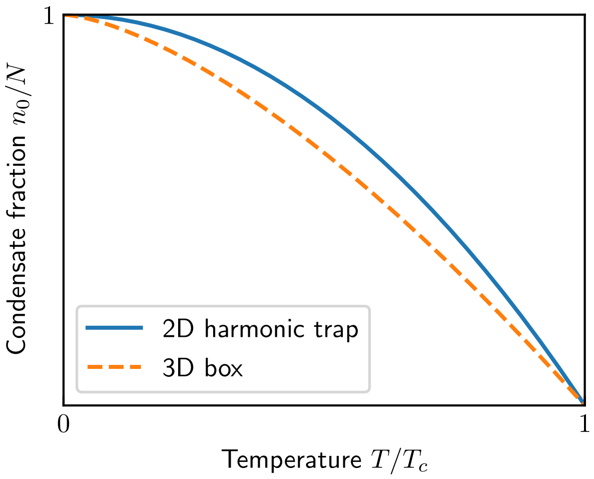

FIGURE 2.3: Condensate fraction as a function of temperature for a 2D harmonic (solid blue line) and a 3D box potential (dashed orange line).

n_0/N will be negligibly small [see Fig. 2.3 showing the condensate fraction n_0/N (dashed orange curve) as a function of T]. This phase transition to a macroscopically occupied bosonic ground state is called Bose-Einstein condensation (BEC). Here we have considered the density of particles N/V to be some fixed number from which the critical temperature can be calculated via equation (2.10). Alternatively, for a given temperature (e.g., room temperature), a critical particle density is obtained from the same equation.

For the case of massive bosons trapped in a 2-dimensional (2D) harmonic potential, which is considered in the following sections on photon BEC, we now proceed analogously to obtain an estimate of a critical temperature (or equivalently, a critical particle number). The energy spectrum of an isotropic 2D harmonic potential is

$$\varepsilon_n = \hbar\Omega(n+1), \tag{2.12}$$

where Ω is the harmonic oscillator frequency. The degeneracy of the n-th energy level is $n+1$ and the gap between the equidistant levels is $\hbar\Omega$. Thus, the density of states is

$$g(\varepsilon) = 2\frac{n+1}{\hbar\Omega} = 2\frac{\varepsilon}{(\hbar\Omega)^2}, \tag{2.13}$$

where a factor of 2 is included to account for the polarization of light (photon helicity).

Again, we separate the total number of particles into two contributions, n_0 and N' for the ground state and all the excited states, respectively

$$N = n_0 + \int_0^\infty \frac{g(\varepsilon)d\varepsilon}{e^{\beta\varepsilon}/z-1} = n_0 + \frac{2}{(\beta\hbar\Omega)^2}\int_0^\infty \frac{x\,dx}{e^x/z-1}, \tag{2.14}$$

where a substitution $x = \beta\varepsilon$ is made in the last equality. Expanding the integrand and integrating term by term gives N' as the following series (function of z)

$$N'(z) = 2\left(\frac{k_B T}{\hbar\Omega}\right)^2 \sum_{m=1}^{\infty} \frac{z^m}{m^2} \tag{2.15}$$

A critical particle number N_c is now obtained when taking the limit $z \to 1$. We get

$$N_c = N'(1) = 2\left(\frac{k_B T}{\hbar\Omega}\right)^2 \zeta(2) = \frac{\pi^2}{3}\left(\frac{k_B T}{\hbar\Omega}\right)^2, \tag{2.16}$$

while the condensate fraction n_0/N has the following temperature dependence [36]

$$\frac{n_0}{N} = 1 - \left(\frac{T}{T_c}\right)^2, \tag{2.17}$$

which is shown in Fig. 2.3 (solid blue curve).

2.3 Properties of equilibrium-like photon condensate

It took seven decades after the theoretical prediction of Bose-Einstein condensation [37] for the first experimental realization of this phenomenon. It was achieved with a very dilute atomic gas cooled down below a critical temperature $T \simeq 170$ nK and under micro-canonical conditions [1]. In contrast, a quasiequilibrium photon condensate, which was realized 15 years later [11], emerges at room temperature (above a critical photon number) and under grand-canonical conditions. Some important properties of this system are discussed in the remainder of this chapter.

2.3.1 Chemical potential of light and Kennard-Stepanov law

It is well known that the chemical potential of black-body radiation is zero [35]. Given that the number of photons in a black cavity changes as a result of absorption and emission events on the cavity walls, there is no constraint that the photon number needs to be conserved and the corresponding Lagrange multiplier, the chemical potential, must be set to zero. However, this vanishing chemical potential is not an inherent property of a photon gas, but a consequence of the fact that matter (walls of the black cavity) is not explicitly included in the description of an equilibrium state of a photon gas inside the cavity. Strictly speaking, since photons do not interact with each other, they cannot achieve equilibrium by themselves [38].

Let us now consider a situation where photons are in a highly reflective cavity filled with some medium consisting of atoms or molecules, which can absorb and emit the photons. A dynamical equilibrium between the photons (γ), excited ($\mathcal{M}_\uparrow$) and ground-state atoms or molecules ($\mathcal{M}_\downarrow$), can be represented by the following "chemical" equation [2]

$$\mathcal{M}_\downarrow + \gamma \rightleftarrows \mathcal{M}_\uparrow. \tag{2.18}$$

At constant temperature and volume (pressure), the equilibrium state corresponds to a minimum in the Helmholtz (Gibbs) free energy X, implying that

$$dX = \sum_i \mu_i dN_i = \sum_i \frac{\partial X}{\partial N_i} dN_i = 0, \tag{2.19}$$

because the changes in temperature and volume (pressure), dT and $dV(dp)$, are zero. Here, dN_i is the change in particle number of species $i = \{\gamma, \downarrow, \uparrow\}$ and μ_i is the corresponding chemical potential. From Eq. (2.18) it follows that $dN_\gamma = dN_\downarrow = -dN_\uparrow$, which inserted into Eq. (2.19) gives the following condition

$$\mu_\gamma + \mu_\downarrow = \mu_\uparrow. \tag{2.20}$$

This replaces the requirement that $\mu_\gamma = 0$ for the case of black-body radiation (or the requirement $dN = 0$ for a system with a single particle type and its number conserved). Therefore, the photon chemical potential is no longer necessarily zero in this scenario and it will depend of the energy gap between the excited and ground-state atoms (molecules).

Such a scenario was used to achieve a quasiequilibrium Bose-Einstein condensation of photons [11]. It involved a highly reflective microcavity filled with a dye solution and photons which interact with the dye molecules [photochemical reaction (2.18)]. The molecule in the ground-state becomes excited by absorbing a photon of frequency ω, as shown in the lower panel of Fig 2.4. The frequency of the bare electronic transition (zero-phonon line) is denoted by ω_{zpl}. The two electronic states of the dye molecule have an additional structure, labeled $S_\downarrow$ and $S_\uparrow$, corresponding to rovibrational states of the lower ($e_i \in S_\downarrow$) and upper manifold ($e_f \in S_\uparrow$). There are multiple pairs (i, f), which correspond to any given transition frequency ω, i.e., those that satisfy the relation

$$e_f - e_i = \hbar\omega - \hbar\omega_{zpl}. \tag{2.21}$$

---

[2] The energy of optical photons is well above thermal energy at room temperature, which makes the conversion of ground-state molecules into excited ones by thermal fluctuations negligible.

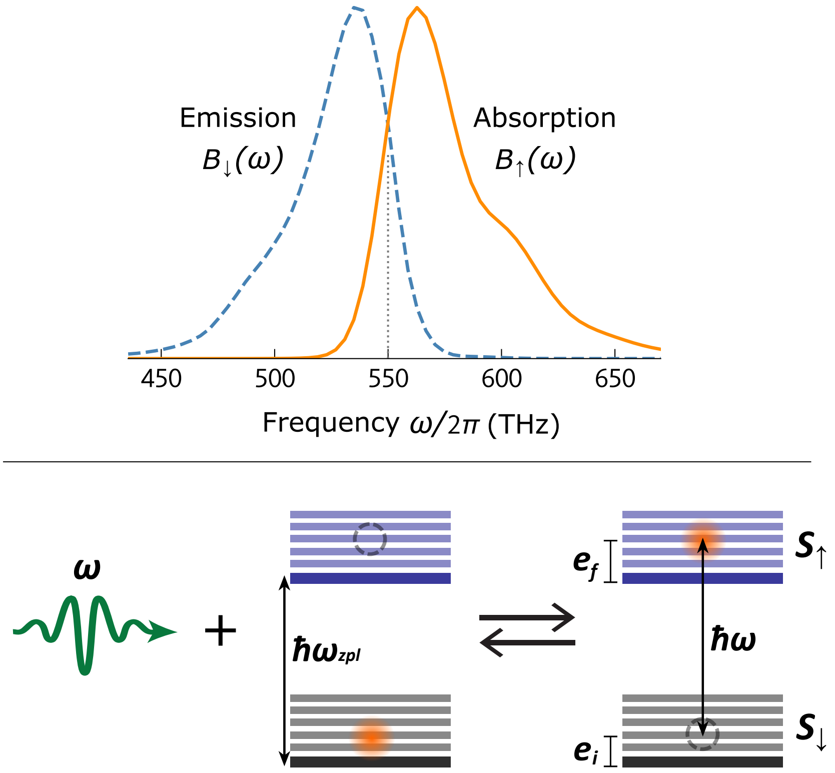

FIGURE 2.4: Upper panel: absorption and fluorescence spectra of a dye solution. Lower panel: photochemical reaction between the photons, the ground-state and the excited-state molecules. The molecule in the ground-state becomes excited by absorbing a photon of frequency ω. The two electronic states of the dye molecule have an additional structure, labeled $S_\downarrow$ and $S_\uparrow$, corresponding to rovibrational states. The frequency of the bare electronic transition (zero-phonon line) is denoted by ω_{zpl}.

The dye solution is characterized by broad absorption and fluorescence spectra (see upper panel of Fig 2.4) and satisfies the Kennard-Stepanov law [10, 39, 40]

$$\frac{B_\downarrow(\omega)}{B_\uparrow(\omega)} = \frac{w_\downarrow}{w_\uparrow} e^{-\beta\hbar(\omega-\omega_{zpl})}, \tag{2.22}$$

where $B_\uparrow(\omega)$ and $B_\downarrow(\omega)$ are the Einstein coefficients of absorption and stimulated emission, respectively, while $w_\downarrow$ and $w_\uparrow$ are the statistical weights corresponding to the rovibronic sublevels of the ground ($\downarrow$) and excited state ($\uparrow$)

$$w_\downarrow = \sum_{i\in S_\downarrow} e^{-\beta e_i}\ ; \quad w_\uparrow = \sum_{i\in S_\uparrow} e^{-\beta e_f}. \tag{2.23}$$

Due to frequent collisions between the dye and the solvent molecules, these rovibronic states of the dye molecules ($S_\uparrow$ and $S_\downarrow$ manifolds in Fig. 2.4) are thermally populated. That is, the corresponding probabilities are given by

$$p_i = \frac{e^{-\beta e_i}}{w_\downarrow}\ ; \quad p_f = \frac{e^{-\beta e_f}}{w_\uparrow}. \tag{2.24}$$

More precisely, these rovibrational states are, to a very good approximation, thermally distributed, because the rovibrational relaxation of dye molecules, resulting from frequent collisions with the solvent molecules and happening at the "thermalization rate" $\kappa_T <$ ps, is much faster than the radiative decay of $S_\uparrow$ (rate at which photons are emitted by the dye molecules, $\kappa_R \lesssim$ ns) [41, 42]. This rate is in turn sufficiently large compared to the photon loss rate κ (rate at which the photons leave the cavity due to various loss mechanisms [3]). That is, the dye molecules absorb and re-emit the photons several times before they leak out of the cavity, resulting in their thermalization to the rovibrational temperature of the dye (room temperature).

In such a case as this (electronic two-level system with rovibronic sublevels), the Einstein coefficients $B_\downarrow(\omega)$ and $B_\uparrow(\omega)$ at a given frequency ω are defined as the averages over all pairs (i, f) that match this transition frequency, i.e. those that satisfy the equation (2.21). Using this condition, it follows that

$$p_f = \frac{e^{-\beta\hbar(\omega-\omega_{zpl})}}{w_\uparrow} e^{-\beta e_i} = \frac{w_\downarrow}{w_\uparrow} e^{-\beta\hbar(\omega-\omega_{zpl})} p_i. \tag{2.25}$$

We then get

$$\frac{B_\downarrow(\omega)}{B_\uparrow(\omega)} = \frac{\sum_{i,f} p_f B_{f\to i}}{\sum_{i,f} p_i B_{f\leftarrow i}} = \frac{w_\downarrow}{w_\uparrow} e^{-\beta\hbar(\omega-\omega_{zpl})}, \tag{2.26}$$

---

[3] Losses happen as a result of nonradiative decay, imperfect mirror reflectivity and optical modes not confined within the cavity.

where the equality $B_{f\to i} = B_{f\leftarrow i}$ has also been used. This concludes the derivation of the Kennard-Stepanov law [42].

In addition to providing a thermalizing environment, dye molecules also act as a particle reservoir for the photons in the sense that photons (γ) are exchanged between the electronic ground ($\downarrow$) and excited state ($\uparrow$) of the molecules, so that the three species are in a dynamic equilibrium and equation (2.20) for the corresponding chemical potentials is satisfied [42]. It follows that the photon fugacity is given by

$$z = e^{\beta\mu_\gamma} = \frac{e^{\beta\mu_\uparrow}}{e^{\beta\mu_\downarrow}}. \tag{2.27}$$

Taking into account that the lowest energies in the $S_\downarrow$ and $S_\uparrow$ manifold are $e_{i=0} = 0$ and $e_{f=0} = \hbar\omega_{zpl}$, respectively (see Fig. 2.4), the partition function of a single dye molecule is given by

$$Z = w_\downarrow e^{\beta\mu_\downarrow} + w_\uparrow e^{-\beta(\hbar\omega_{zpl}-\mu_\uparrow)}. \tag{2.28}$$

It follows that the probability ratio to find a dye molecule in the excited vs. ground state is

$$\frac{P_\uparrow}{P_\downarrow} = \frac{w_\uparrow e^{-\beta(\hbar\omega_{zpl}-\mu_\uparrow)}}{w_\downarrow e^{\beta\mu_\downarrow}} = \frac{f}{1-f}, \tag{2.29}$$

where f is the fraction of excited dye molecules in the solution. Inserting this result into Eq. (2.27), we get the expression for photon fugacity

$$z = \frac{w_\downarrow}{w_\uparrow}\frac{f}{1-f}e^{\beta\hbar\omega_{zpl}}, \tag{2.30}$$

where $w_\downarrow/w_\uparrow$ is a frequency-independent proportionality factor. Therefore, in dynamical equilibrium, the ratio of the number of excited and ground-state dye molecules determines the chemical potential of photons, as well as the energy gap $\hbar\omega_{zpl}$ of the electronic transition.

2.3.2 Grand-canonical number fluctuations in photon BEC

If the chemical potential μ_γ of photons is fixed and determined by the ratio $f/(1-f)$, as explained above, the number of photons is then allowed to fluctuate around its average value set by μ_γ. If the temperature is fixed as well, this corresponds to a grand-canonical ensemble. When a photon gets absorbed by a dye molecule, it leaves the system (photon gas) and "enters the reservoir" (excited molecules) [4]. In a lot of physical systems a choice of ensemble is merely a matter of convenience, because relative fluctuations in various observables vanish in all of them in the thermodynamic limit. In the case of BECs, however, the grand-canonical treatment predicts fluctuations on the order of the total particle number. This is derived as follows.

---

[4] The total number of photons and excited molecules should be conserved. Given the presence of mirror losses, this is achieved via steady pumping with an external laser, which compensates these losses.

The grand-canonical partition function for a system of non-interacting bosons is

$$Z_G = \prod_i \sum_{N=0}^{\infty} e^{\beta N(\mu-\varepsilon_i)}, \tag{2.31}$$

where ε_i are the eigenenergies. The corresponding free energy is the grand potential

$$\Omega_G = -k_B T \ln Z_G, \tag{2.32}$$

from which the ensemble average of the particle number $\langle N\rangle$ is calculated via

$$\langle N\rangle = -\left(\frac{\partial \Omega_G}{\partial \mu}\right)_{T,V}, \tag{2.33}$$

while the variance $(\Delta N)^2$ (fluctuations in particle number) is given by

$$(\Delta N)^2 = \langle N^2\rangle - \langle N\rangle^2 = k_B T\left(\frac{\partial\langle N\rangle}{\partial \mu}\right)_{T,V} = -k_B T\left(\frac{\partial^2 \Omega_G}{\partial \mu^2}\right)_{T,V} \tag{2.34}$$

Given that the system is non-interacting, to each eigenstate i corresponds a separate grand potential Ω_G^i given by

$$\Omega_G^i = -k_B T \ln\left(\sum_{N=0}^{\infty} e^{\beta N(\mu-\varepsilon_i)}\right) = k_B T \ln\left(1 - e^{\beta(\mu-\varepsilon_i)}\right). \tag{2.35}$$

It follows that the particle number variance in that state is

$$(\Delta n_i)^2 = \langle n_i^2\rangle - \langle n_i\rangle^2 = -k_B T\left(\frac{\partial^2 \Omega_G^i}{\partial \mu^2}\right)_{T,V} = \frac{e^{\beta(\varepsilon_i-\mu)}}{(e^{\beta(\varepsilon_i-\mu)-1})^2} = \langle n_i\rangle(\langle n_i\rangle + 1). \tag{2.36}$$

We see that for any given state i, the particle number n_i fluctuates on the order of its mean value $\langle n_i\rangle$. In particular, in the case of a Bose-Einstein condensate (when the total particle number N exceeds a critical value N_c), we get that the number fluctuations in the ground state are on the order of the total particle number

$$\Delta n_0 \simeq \langle n_0\rangle \simeq N. \tag{2.37}$$

The validity of grand-canonical ensemble lies on the assumption that the reservoir is much larger than the system. Therefore, the size of particle number fluctuations (and the relevance of grand-canonical statistics) is expected to increase with the size of the particle reservoir relative to the system size. This dependence was investigated in Ref. [18] both theoretically and experimentally using a Hanbury-Brown-Twiss setup [43]. Changing the type of dye solution (thus changing its transition frequency), as well as the dye concentration, allowed the effective reservoir size to be varied over three orders of magnitude. Large number fluctuations of the order of the total particle number and extending deep into the condensed phase were observed in the case of a sufficiently large effective reservoir. As expected, it was also found that the relative fluctuations gradually vanish as the reservoir size is reduced.

Chapter 3

System and model

The system in which the equilibrium-like Bose-Einstein condensation of photons was first observed [11] is schematically illustrated in Fig. 3.1. It shows a single longitudinal photonic mode within a cavity filled with an organic dye solution and pumped by an external laser beam. The separation between the cavity mirrors is roughly a micrometer, which results in a large spacing between adjacent longitudinal photonic modes, so that at room temperature, only one of these modes, specified by its longitudinal quantum number q (as shown in the figure) is coupled to the electronic transition of the dye. Here, q is a positive integer in the boundary condition

$$k_z(r) = \frac{q\pi}{D(r)}, \tag{3.1}$$

where $r = \sqrt{x^2 + y^2}$ is the distance from the optical axis, $k_z(r)$ is the longitudinal component of the photon wave vector $\vec{k}$ and the separation $D(r)$ between the spherically curved

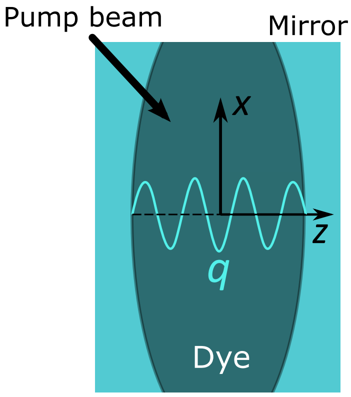

FIGURE 3.1: Schematically illustrated experimental setup containing an optical microresonator filled with a dye solution and pumped with an external laser.

mirrors (with radius of curvature R) is given by (see the left panel of Fig. 3.2)

$$D(r) = D_0 - 2(R - \sqrt{R^2 - r^2}). \tag{3.2}$$

The photon energy is given by the dispersion relation

$$E = \hbar\tilde{c}|\vec{k}| = \hbar\tilde{c}\sqrt{[k_z(r)]^2 + k_r^2} \approx \hbar\tilde{c}\left(k_z + \frac{k_r^2}{2k_z}\right), \tag{3.3}$$

where $\tilde{c}$ is the speed of light in the dye medium, $k_r = \sqrt{k_x^2 + k_y^2}$ is the transverse component of the wave vector and a paraxial approximation $k_r \ll k_z$ was used to obtain the last equality. This approximation is used when the rays of light make small angles to the optical axis and lie close to it throughout the system. In the experimental setup discussed here, the optical axis is the z-axis and therefore, the small-angle requirement means $k_r/k_z \ll 1$. This is satisfied given that $k_r/k_z \sim D_0/r_{max} \simeq 10^{-3}$ [10]. Inserting equations (3.1) and (3.2) into the dispersion relation (3.3) and using the fact that $r/R \ll 1$ [1], we obtain an effective 2-dimensional harmonic potential for the photons in the transverse direction $\vec{r} = (x, y)$

$$E \approx m_{ph}\tilde{c}^2 + \frac{(\hbar k_r)^2}{2m_{ph}} + \frac{1}{2}m_{ph}\,\Omega^2 r^2, \tag{3.4}$$

with $\Omega = \tilde{c}\sqrt{2/D_0R}$ as the harmonic oscillator frequency and m_{ph} as the effective photon mass, which is nonzero due to the presence of a frequency cutoff, $\tilde{c}|\vec{k}| \geq \tilde{c}k_z(0)$. The corresponding "rest mass" term in Eq. 3.4 is given by

$$E_{z,0} = m_{ph}\tilde{c}^2 = \hbar\tilde{c}k_z(0). \tag{3.5}$$

By introducing variation in the effective shape of the mirror [2], different kinds of trapping potentials for the photons can be created. One particular method of doing this [30] is elaborated on in Chapter 6. A sketch of a such a reshaped mirror corresponding to a double-well potential for the photons, is shown on the right panel of Fig. 3.2. The effective mirror separation $D(r)$ is no longer given by equation (3.2). Instead, the optical wavelength now has two local maxima, corresponding to local minima in the effective potential. Inserting the condition (3.1) on the wave vector into the general expression for the photon energy (3.3),

---

[1] This approximation is valid given that $r < 1\,\mathrm{mm}$ is much smaller than the radius of the spherically curved mirrors $R \simeq 1\,\mathrm{m}$ [10].

[2] We use the word "effective" here, because it is not necessary to physically deform the mirror in order to produce a different effective potential for the photons. The only requirement is that a variation in the optical wavelength is produced via some technique, like the one mentioned in Chapter 6.

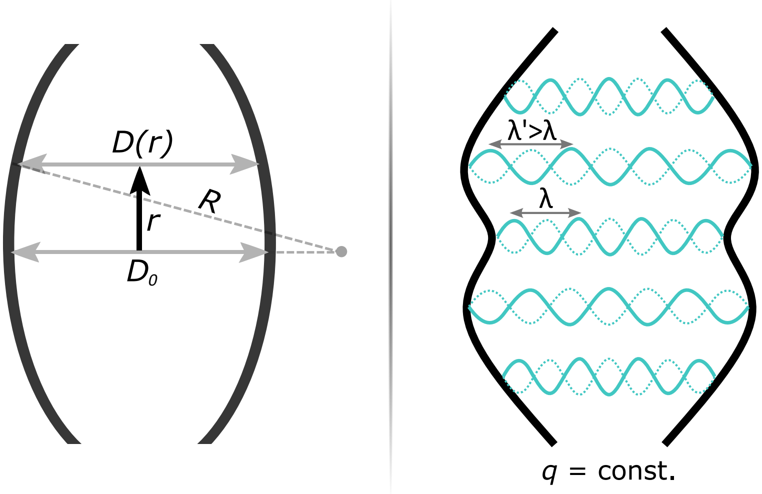

FIGURE 3.2: Left panel: spherically curved mirrors (with radius of curvature R) separated by $D(r)$, which depends on the distance r from the optical axis. Right panel: reshaping of the mirrors produces a different potential. The requirement that the boundary conditions imposed by the cavity are locally satisfied, results in a variation of the optical wavelength, and correspondingly, the effective potential experienced by the photons.

we get

$$\begin{aligned} E_{eff}(r) &\approx \hbar\tilde{c}\left(k_z(r) + \frac{k_r^2}{2k_z(r)}\right) \\ &= \hbar\tilde{c}\left(\frac{q\pi}{D(r)} + \frac{k_r^2\,D(r)}{2q\pi}\right) \\ &= m_{ph}\tilde{c}^2 + \frac{(\hbar k_r)^2}{2m_{ph}} + \sum_{n=1}^{4} C_n(0)r^n + \mathcal{O}(5), \end{aligned} \tag{3.6}$$

where an expansion in $r/R \ll 1$ is made in the last equality. By tuning the system parameters, the expansion coefficients $C_n(0)$ can be achieved which correspond to a double-well potential, for instance.

In the case of spherically curved mirrors the transverse photonic modes $\psi_i(\vec{r})$ (Fig. 3.3) are the eigenfunctions of the two-dimensional harmonic potential. They are characterized by a pair of harmonic oscillator quantum numbers in x and y direction, $i = (\nu_x, \nu_y)$, and have energies $E_i = \hbar[\Omega_x(\nu_x + 1/2) + \Omega_y(\nu_y + 1/2)]$ with oscillator frequencies Ω_x and Ω_y. In the following, we assume Ω_x and Ω_y to be almost identical, $\Omega_x \equiv \Omega$ and $\Omega_y = 0.99\,\Omega$. This slight anisotropy of the trap is a realistic assumption and is required for eliminating

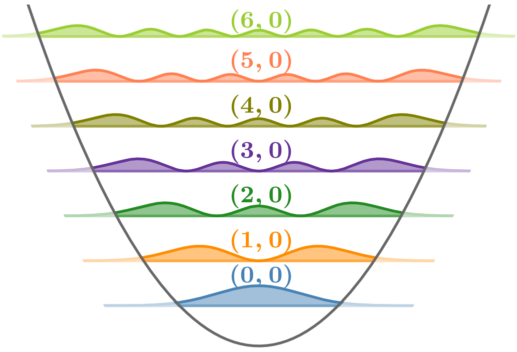

FIGURE 3.3: Photon mode densities $|\psi_{n_x,n_y}(x)|^2$ projected onto the x axis. For simplicity, only modes $(n_x, 0)$, with nodes only along x direction, are shown.

the coherent mixing of otherwise degenerate modes i [3]. The harmonic oscillator length d associated with Ω is used as a natural unit of length. The total energy of the cavity mode i is then given by $\varepsilon_i = \hbar\omega_i = E_i + E_{z,0}$, where $E_{z,0}$ is defined in Eq. 3.5. As already mentioned, other photonic modes corresponding to different potential landscapes can also be considered and realized experimentally. This is done in Chapter 6 for the case of an asymmetric double-well potential.

3.1 Master equation

The system can be modeled by the master equation [19, 44] for the state characterized by the electronic degrees of freedom of the dye molecules j as well as the photon modes i

$$\begin{aligned}\dot{\rho} \;=\; & -i\left[\sum_i \delta_i a_i^\dagger a_i, \rho\right] + \left\{\sum_i \kappa\mathcal{L}[a_i] + \sum_j \left(P_j\mathcal{L}[\sigma_j^+] + \Gamma\mathcal{L}[\sigma_j^-]\right)\right\}\rho \\ & + \left\{\sum_{i,j}\left(R_\uparrow^{i,j}\mathcal{L}[a_i\sigma_j^+] + R_\downarrow^{i,j}\mathcal{L}[a_i^\dagger\sigma_j^-]\right)\right\}\rho, \end{aligned} \tag{3.7}$$

where $\mathcal{L}\left[X\right]\rho = X\rho X^\dagger - \frac{1}{2}\left\{X^\dagger X, \rho\right\}$ are the standard Lindblad terms. The various processes contained within this master equation are schematically illustrated in Fig. 3.4. Each dye molecule has its position (labeled by j) in a two-dimensional space given by

---

[3] In any real experiment, there will be a slight anisotropy to break the degeneracy, resulting in a definite set of photon modes. In the isotropic case, however, any orthonormal set of linear combinations of modes within a degenerate subspace is an equally valid choice and choosing any particular set would be arbitrary. Therefore, to avoid any ambiguity, we choose the slightly anisotropic case in our simulations.

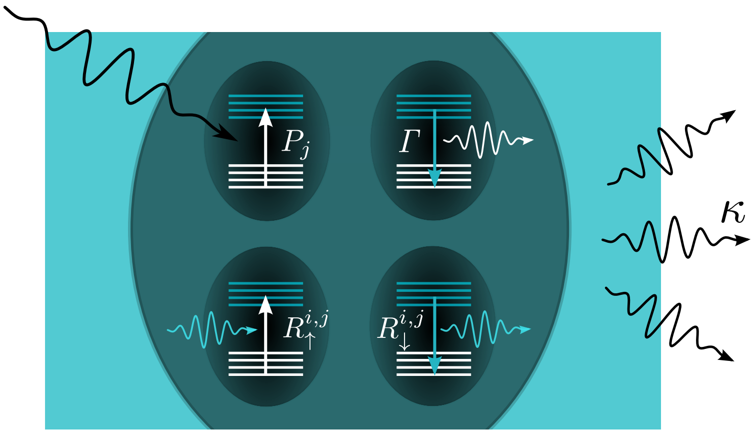

FIGURE 3.4: Illustration of the model showing all of the processes contained in the dissipative part of the Lindblad master equation.

the transverse directions (perpendicular to the optical axis of the cavity), $\vec{r} = (x, y)$. Its electronic states are modeled as a two-level system with the corresponding raising and lowering operators $\sigma_j^{\pm} = (\sigma_j^x \pm \sigma_j^y)/2$. To each photon mode i corresponds the creation (annihilation) operator $a_i^{\dagger}$ (a_i), while $\delta_i = \omega_i - \omega_{zpl}$ is its frequency relative to the splitting of the two-level system (zero-phonon line) ω_{zpl}. The presence of the detunings δ_i (as opposed to the mode frequencies ω_i) in the master equation, results from a shift to a frame rotating with the zero-phonon frequency. The rate of spontaneous losses, where the dye molecules emit photons into non-cavity modes [4], is given by Γ. The photon-cavity lifetime is finite, due to loss mechanisms (like the mirror losses), which happen at a rate κ, assumed to be mode independent. These are processes where photons leave the system (photon gas) without going into the particle reservoir (electronic excitations of the dye molecules). Therefore, the system needs to be (continuously) pumped with an external laser in order to stabilize the average photon number. The corresponding spatially dependent pump rate is denoted by $P_j \equiv P(\vec{r})$.

As mentioned in Chapter 2, the rovibrational states of the dye molecules in a solution relax rapidly to equilibrium (the corresponding rate is much larger than the rate of radiative decay). As a result, their occupation numbers need not to be taken into account explicitly. Instead, this effect is described via the rates $R_{\uparrow,\downarrow}^{i,j} = \rho |\psi_i(\vec{r_j})|^2 R_{\uparrow,\downarrow}^{i}$. They depend on position $\vec{r}_j$, the number density of the molecules ρ and the frequency ω_i of mode i, through the absorption (↑) and emission (↓) rates $R_{\uparrow,\downarrow}^{i}$, which characterize the dye solution. They satisfy the Kennard-Stepanov law [10, 39, 40]. That is, their ratio is proportional to the

---

[4] We define cavity modes as all the modes corresponding to a single longitudinal mode number q, which populate the cavity and are considered explicitly in the master equation (rate equations). All the other modes are called non-cavity modes.

Boltzman factor

$$R^i_\downarrow / R^i_\uparrow = C e^{-\beta\hbar(\omega_i - \omega_{zpl})}, \tag{3.8}$$

enabling the thermalization of photon gas. Here, C is a frequency-independent proportionality factor. The coupling between the dye molecules and the photons is only present in the dissipative part of the master equation. This approximation is justified by the very broad emission and absorption spectra of the dye [19, 44] (see upper panel of Fig. 2.4).

3.2 Derivation of the rate equations from the master equation

From the master equation a closed system of semiclassical equations of motion can be derived [19, 31, 44] for the photon mode populations $n_i = \langle a_i^\dagger a_i \rangle$, and the fraction $f(\vec{r}) \equiv f_j$ of excited dye molecules at position $\vec{r}$. The quantity f_j has the following relation to the Pauli operators

$$f_j = \frac{1 + \langle \sigma_j^z \rangle}{2} = \langle \sigma_j^+ \sigma_j^- \rangle\,. \tag{3.9}$$

The expectation value of an observable Q is given by $\langle Q \rangle = \mathrm{Tr}(Q\rho)$, where ρ is the density matrix. The observables cosidered here are $a_i^\dagger a_i$ and σ_j^z. In the following derivation of the rate equations for $\langle a_i^\dagger a_i \rangle$ and $\langle \sigma_j^z \rangle$, we use the freedom to interchange operators which commute and to perform cyclic permutations under the trace operator. We also use the following commutation relations

$$\begin{aligned} [a_i, a_j^\dagger] =&\ \delta_{ij}, \\ [\sigma_j^z, \sigma_j^\pm] =&\ \pm\sigma_j^\pm. \end{aligned} \tag{3.10}$$

Using the Lindblad master equation (3.7), we find that the equation for n_i is, term by term ($=^m$ is the m^{th} term in the master equation):

$$\begin{aligned}
\frac{\mathrm{d}\langle a_i^\dagger a_i\rangle}{\mathrm{d}t} &=^1 -i\sum_m \delta_m \,\mathrm{Tr}\left[(a_i^\dagger a_i)(a_m^\dagger a_m)\rho - (a_i^\dagger a_i)\rho(a_m^\dagger a_m)\right] = 0 \\
\frac{\mathrm{d}\langle a_i^\dagger a_i\rangle}{\mathrm{d}t} &=^2 -\frac{\kappa}{2}\sum_m \mathrm{Tr}\left[(a_i^\dagger a_i)(a_m^\dagger a_m)\rho + (a_i^\dagger a_i)\rho(a_m^\dagger a_m) - 2(a_i^\dagger a_i)a_m\rho a_m^\dagger\right] \\
&=^2 -\frac{\kappa}{2}\sum_{m\neq i} \mathrm{Tr}\left[(a_i^\dagger a_i)(a_m^\dagger a_m)\rho + (a_i^\dagger a_i)(a_m^\dagger a_m)\rho - 2(a_i^\dagger a_i)(a_m^\dagger a_m)\rho\right] \\
&\quad\; -\frac{\kappa}{2}\,\mathrm{Tr}\left[(a_i^\dagger a_i)(a_i^\dagger a_i)\rho + (a_i^\dagger a_i)(a_i^\dagger a_i)\rho - 2a_i^\dagger a_i^\dagger a_i a_i\rho\right] \\
&=^2 -\kappa\,\mathrm{Tr}\left[a_i^\dagger[a_i, a_i^\dagger]a_i\rho\right] \\
&=^2 -\kappa\,\mathrm{Tr}\left[a_i^\dagger a_i\rho\right] = -\kappa\left\langle a_i^\dagger a_i\right\rangle = -\kappa n_i \\
\frac{\mathrm{d}\langle a_i^\dagger a_i\rangle}{\mathrm{d}t} &=^5 -\sum_{m,j}\frac{R_\uparrow^{i,j}}{2}\,\mathrm{Tr}\left[(a_i^\dagger a_i)(a_m^\dagger a_m)(\sigma_j^-\sigma_j^+)\rho + (a_i^\dagger a_i)\rho(a_m^\dagger a_m)(\sigma_j^-\sigma_j^+) - 2a_i^\dagger a_i a_m\sigma_j^+\rho a_m^\dagger\sigma_j^-\right] \\
&=^5 -\sum_{m,j}\frac{R_\uparrow^{i,j}}{2}\,\mathrm{Tr}\left[(a_i^\dagger a_i)(a_m^\dagger a_m)\rho(\sigma_j^-\sigma_j^+) + (a_m^\dagger a_m)(a_i^\dagger a_i)\rho(\sigma_j^-\sigma_j^+) - 2a_m^\dagger a_i^\dagger a_i a_m\rho(\sigma_j^-\sigma_j^+)\right] \\
&=^5 -\sum_{j}\frac{R_\uparrow^{i,j}}{2}\,\mathrm{Tr}\left[(a_i^\dagger a_i)(a_i^\dagger a_i)\rho(\sigma_j^-\sigma_j^+) + (a_i^\dagger a_i)(a_i^\dagger a_i)\rho(\sigma_j^-\sigma_j^+) - 2a_i^\dagger a_i^\dagger a_i a_i\rho(\sigma_j^-\sigma_j^+)\right] \\
&=^5 -\sum_j R_\uparrow^{i,j}\,\mathrm{Tr}\left[a_i^\dagger[a_i, a_i^\dagger]a_i(\sigma_j^-\sigma_j^+)\rho\right] \\
&=^5 -\sum_j R_\uparrow^{i,j}\,\mathrm{Tr}\left[(a_i^\dagger a_i)(\sigma_j^-\sigma_j^+)\rho\right] \\
&=^5 -\sum_j R_\uparrow^{i,j} n_i(1-f_j) \\
\frac{\mathrm{d}\langle a_i^\dagger a_i\rangle}{\mathrm{d}t} &=^6 -\sum_{m,j}\frac{R_\downarrow^{i,j}}{2}\,\mathrm{Tr}\left[(a_i^\dagger a_i)(a_m a_m^\dagger)(\sigma_j^+\sigma_j^-)\rho + (a_i^\dagger a_i)\rho(a_m a_m^\dagger)(\sigma_j^+\sigma_j^-) - 2a_i^\dagger a_i a_m^\dagger\sigma_j^-\rho a_m\sigma_j^+\right] \\
&=^6 -\sum_{j}\frac{R_\downarrow^{i,j}}{2}\,\mathrm{Tr}\left[(a_i^\dagger a_i)(a_i a_i^\dagger)\rho(\sigma_j^+\sigma_j^-) + (a_i a_i^\dagger)(a_i^\dagger a_i)\rho(\sigma_j^+\sigma_j^-) - 2(a_i a_i^\dagger)(a_i a_i^\dagger)\rho(\sigma_j^+\sigma_j^-)\right] \\
&=^6 -\sum_{j}\frac{R_\downarrow^{i,j}}{2}\,\mathrm{Tr}\left[[a_i^\dagger, a_i]a_i a_i^\dagger\rho\sigma_j^+\sigma_j^- + a_i a_i^\dagger[a_i^\dagger, a_i]\rho\sigma_j^+\sigma_j^-\right] \\
&=^6 \sum_{j}\frac{R_\downarrow^{i,j}}{2}\,\mathrm{Tr}\left[2a_i a_i^\dagger\rho\sigma_j^+\sigma_j^-\right] \\
&=^6 \sum_j R_\downarrow^{i,j}(n_i+1)f_j
\end{aligned}$$

To obtain a closed system of equations, in the last equation for each term we used a factorization (semiclassical approximation)

$$\begin{aligned} \langle a_i^\dagger a_i \sigma_j^+ \sigma_j^- \rangle = \langle a_i^\dagger a_i \rangle \langle \sigma_j^+ \sigma_j^- \rangle &= \; n_i f_j, \\ \langle a_i^\dagger a_i \sigma_j^- \sigma_j^+ \rangle = \langle a_i^\dagger a_i \rangle \langle \sigma_j^- \sigma_j^+ \rangle &= \; n_i (1 - f_j), \end{aligned} \tag{3.11}$$

where the expectation values of products of observables $a_i^\dagger a_i$ and $\sigma_j^\pm \sigma_j^\mp$ are replaced by the product of expectation values. In other words, the state of the photons is assumed to be uncorrelated with the state of the dye molecules.

Collecting together all of the terms, we get the equation of motion for n_i

$$\frac{\mathrm{d}n_i}{\mathrm{d}t} = -\kappa n_i - \sum_j R_\uparrow^{i,j} n_i (1 - f_j) + \sum_j R_\downarrow^{i,j} (n_i + 1) f_j. \tag{3.12}$$

Analogously, the rate equation for $\langle\sigma_j^z\rangle$ is, term by term

$$\begin{aligned}
\frac{\mathrm{d}\langle\sigma_j^z\rangle}{\mathrm{d}t} &=^3 -\frac{P_j}{2}\,\mathrm{Tr}\left[\sigma_j^z(\sigma_j^-\sigma_j^+)\rho+\sigma_j^z\rho(\sigma_j^-\sigma_j^+)-2\sigma_j^z\sigma_j^+\rho\sigma_j^-\right]\\
&=^3 -\frac{P_j}{2}\,\mathrm{Tr}\left[\sigma_j^z(\sigma_j^-\sigma_j^+)\rho+(\sigma_j^-\sigma_j^+)\sigma_j^z\rho-2\sigma_j^-\sigma_j^z\sigma_j^+\rho\right]\\
&=^3 -\frac{P_j}{2}\,\mathrm{Tr}\left[[\sigma_j^z,\sigma_j^-]\sigma_j^+\rho+\sigma_j^-[\sigma_j^+,\sigma_j^z]\rho\right]\\
&=^3 -P_j\,\mathrm{Tr}\left[-\sigma_j^-\sigma_j^+\rho-\sigma_j^-\sigma_j^+\rho\right]\\
&=^3 2P_j\,\langle\sigma_j^-\sigma_j^+\rangle\\
&=^3 2P_j(1-f_j)\\
\frac{\mathrm{d}\langle\sigma_j^z\rangle}{\mathrm{d}t} &=^4 -\frac{\Gamma}{2}\,\mathrm{Tr}\left[\sigma_j^z(\sigma_j^+\sigma_j^-)\rho+\sigma_j^z\rho(\sigma_j^+\sigma_j^-)-2\sigma_j^z\sigma_j^-\rho\sigma_j^+\right]\\
&=^4 -\frac{\Gamma}{2}\,\mathrm{Tr}\left[\sigma_j^z(\sigma_j^+\sigma_j^-)\rho+(\sigma_j^+\sigma_j^-)\sigma_j^z\rho-2\sigma_j^+\sigma_j^z\sigma_j^-\rho\right]\\
&=^4 -\frac{\Gamma}{2}\,\mathrm{Tr}\left[[\sigma_j^z,\sigma_j^+]\sigma_j^-\rho+\sigma_j^+[\sigma_j^-,\sigma_j^z]\rho\right]\\
&=^4 -\Gamma\,\mathrm{Tr}\left[(\sigma_j^+\sigma_j^-)\rho+(\sigma_j^+\sigma_j^-)\rho\right]\\
&=^4 -2\Gamma f_j\\
\frac{\mathrm{d}\langle\sigma_j^z\rangle}{\mathrm{d}t} &=^5 -\sum_i\frac{R_\uparrow^{i,j}}{2}\,\mathrm{Tr}\left[\sigma_j^z a_i^\dagger\sigma_j^- a_i\sigma_j^+\rho+\sigma_j^z\rho a_i^\dagger\sigma_j^- a_i\sigma_j^+-2\sigma_j^z a_i\sigma_j^+\rho a_i^\dagger\sigma_j^-\right]\\
&=^5 \sum_i 2R_\uparrow^{i,j}\,\langle(a_i^\dagger a_i)(\sigma_j^-\sigma_j^+)\rangle\\
&=^5 \sum_i 2R_\uparrow^{i,j}n_i(1-f_j)\\
\frac{\mathrm{d}\langle\sigma_j^z\rangle}{\mathrm{d}t} &=^6 -\sum_i\frac{R_\downarrow^{i,j}}{2}\,\mathrm{Tr}\left[\sigma_j^z a_i\sigma_j^+ a_i^\dagger\sigma_j^-\rho+\sigma_j^z\rho a_i\sigma_j^+ a_i^\dagger\sigma_j^--2\sigma_j^z a_i^\dagger\sigma_j^-\rho a_i\sigma_j^+\right]\\
&=^6 -\sum_i 2R_\downarrow^{i,j}\,\langle(a_i^\dagger a_i+1)(\sigma_j^+\sigma_j^-)\rangle\\
&=^6 -\sum_i 2R_\downarrow^{i,j}(n_i+1)f_j
\end{aligned}$$

Again, we collect together all of the terms to obtain the equation of motion for f_j

$$\frac{\mathrm{d}f_j}{\mathrm{d}t}=\frac{1}{2}\frac{\mathrm{d}\langle\sigma_j^z\rangle}{\mathrm{d}t}=P_j(1-f_j)-\Gamma f_j+\sum_i R_\uparrow^{i,j}n_i(1-f_j)-\sum_i R_\downarrow^{i,j}(n_i+1)f_j. \tag{3.13}$$

Finally, using the substitution

$$\begin{aligned}
R_\uparrow^{i,j} &=\rho|\psi_i(\vec{r_j})|^2R_\uparrow^i,\\
R_\downarrow^{i,j} &=\rho|\psi_i(\vec{r_j})|^2R_\downarrow^i,
\end{aligned} \tag{3.14}$$

in equations (3.12) and (3.13), we obtain a set of coupled rate equations

$$\begin{aligned} \dot{n}_i &= -\kappa n_i + (n_i+1)R_\downarrow^i \rho\, G_i - n_i R_\uparrow^i \rho\,(1-G_i), \qquad (3.15) \\ \dot{f}(\vec{r}) &= [1-f(\vec{r})](P(\vec{r}) + \sum_i R_\uparrow^i |\psi_i(\vec{r})|^2 n_i) \\ &\quad - f(\vec{r})[\Gamma + \sum_i R_\downarrow^i |\psi_i(\vec{r})|^2 (n_i+1)]. \qquad (3.16) \end{aligned}$$

Here we have introduced a so-called gain [5] of mode i, which is quantified by its overlap with the fraction $f(\vec{r}) \in [0,1]$ of excited dye molecules,

$$G_i[f(\vec{r})] = \int |\psi_i(\vec{r})|^2 f(\vec{r})\, d\vec{r} \;\in [0,1]. \qquad (3.17)$$

We proceed to explain the meaning of the various terms in the rate equations. In the first equation (3.15), we see that the number of photons in a given mode i can increase due to both stimulated and spontaneous emission, thus the corresponding change is proportional to (n_i+1), as well as the emission rate $R_\downarrow^i$ and the density of excited molecules in the spatial region of the mode, given by $\rho\, G_i$. A decrease in n_i happens as a result of absorption by the dye molecules and the corresponding term is proportional to the number of photons n_i available to be absorbed, as well as the absorption rate $R_\uparrow^i$ and the density of ground-state molecules in the spatial region of the mode $\rho\,(1-G_i)$. Photons also escape through mirror transmission, which is incorporated by the term $-\kappa n_i$. In the second rate equation (3.16) the number of excited molecules increase (decrease) by absorbing (emitting) a photon and the corresponding absorption and emission terms are given by $\sum_i R_\uparrow^i |\psi_i(\vec{r})|^2 n_i$ and $\sum_i R_\downarrow^i |\psi_i(\vec{r})|^2 (n_i+1)$, respectively. A positive change in $f(\vec{r})$ also happens as a result of pumping the ground-state molecules, incorporated by the term $[1-f(\vec{r})]P(\vec{r})$, whereas spontaneous emission into non-cavity modes, given by $f(\vec{r})\Gamma$ contributes to a negative change in $f(\vec{r})$.

3.3 Phenomenological quasi-derivation of the rate equations

Equations (3.15) and (3.16) can be understood intuitively as an extension of the familiar rate equation applied to an electronic transition (two-level system) of an atom or a molecule. They contain three processes (absorption, stimulated and spontaneous emission) with the corresponding Einstein coefficients (proportional to the rates of each process) [45]. This rate equation for the average number of excited molecules $N_\uparrow = \int d\vec{r}\, f(\vec{r})$ reads

---

[5] This quantity is proportional to the usual definition of the gain as the measure of the difference between stimulated emission and absorption. For simplicity, we refer to it as the gain throughout the manuscript.

$$\dot{N}_\uparrow = B_\uparrow (N - N_\uparrow)\,\rho_\omega - B_\downarrow N_\uparrow\,\rho_\omega - A_\downarrow N_\uparrow, \tag{3.18}$$

where N is the total number of molecules, $B_\uparrow$, $B_\downarrow$ and $A_\downarrow$ are the Einstein coefficients of absorption, stimulated and spontaneous emission, respectively, while ρ_ω is the spectral energy density of the radiation field at the frequency ω of the electronic transition. This quantity can be decomposed as $\rho_\omega = u_\omega n_\omega$, where n_ω is the average number of photons with frequency ω, while u_ω is the spectral energy density per photon. The transition frequency ω of the two-level system can be understood as the previously defined zero-phonon frequency ω_{zpl}. The absorption of photons increases the number of excited molecules and the corresponding term $B_\uparrow(N - N_\uparrow)\,\rho_\omega$ depends on the number of ground-state molecules $N - N_\uparrow$, available to be excited. Similarly, the two emission terms are proportional to the number of excited molecules $N_\uparrow$ and affect a negative change in it. The terms corresponding to processes induced by electromagnetic radiation (absorption and stimulated emission) also depend on the spectral energy density ρ_ω.

Using the identity $A_\downarrow / B_\downarrow = u_\omega$, equation (3.18) can be rewritten in the form

$$\dot{N}_\uparrow = B_\uparrow (N - N_\uparrow)\, u_\omega n_\omega - B_\downarrow N_\uparrow\, u_\omega (n_\omega + 1). \tag{3.19}$$

If we now consider the case where the two-level system has a rovibrational substructure, we need to sum over all the transitions between different rovibrational states of the ground and the excited electronic levels that contribute to a change in $N_\uparrow$. These transitions correspond to absorption and emission of photon modes i, with a quasi-continuous spectrum ε_i. We switch to a more convenient notation,

$$\begin{aligned} n_\omega &\to n_i, \\ u_\omega &\to u_i, \end{aligned} \tag{3.20}$$

and the Einstein coefficients are now also frequency dependent

$$\begin{aligned} B_\uparrow &\to B_\uparrow^i, \\ B_\downarrow &\to B_\downarrow^i. \end{aligned} \tag{3.21}$$

If we allow for spatially dependent molecular excitations and introduce driven-dissipative conditions, i.e., pumping with rate $P(\vec{r})$ and spontaneous loss into other modes (rate Γ), the final equation describing the dynamics of $\mathcal{N}_\uparrow(\vec{r})$ reads

$$\dot{\mathcal{N}}_\uparrow(\vec{r}) = P(\vec{r})\mathcal{N}_\downarrow(\vec{r}) - \Gamma \mathcal{N}_\uparrow(\vec{r}) + \mathcal{N}_\downarrow(\vec{r}) \sum_i B_\uparrow^i u_i(\vec{r}) n_i - \mathcal{N}_\uparrow(\vec{r}) \sum_i B_\downarrow^i u_i(\vec{r})(n_i + 1), \tag{3.22}$$

where $u_i(\vec{r})$ is now a spatially dependent spectral energy density per photon at frequency

ω_i and $\mathcal{N}_\uparrow(\vec{r})$ is the number density of excited molecules at position $\vec{r}$. The latter can be written as $\mathcal{N}_\uparrow(\vec{r}) = \rho f(\vec{r})$, where ρ is the total density of dye molecules and $f(\vec{r})$ is their excited fraction. Likewise, the number density of ground state molecules is $\mathcal{N}_\downarrow(\vec{r}) = \rho\{1 - f(\vec{r})\}$.

The corresponding rate equation for the average photon mode occupations n_i, including the loss process with rate κ is

$$\dot{n}_i = -\kappa n_i + (n_i + 1) B^i_\downarrow \int u_i(\vec{r}) N_\uparrow(\vec{r})\, d\vec{r} - n_i B^i_\uparrow \int u_i(\vec{r}) N_\downarrow(\vec{r})\, d\vec{r}, \tag{3.23}$$

where a sum is taken over all the points in space where a change in $N_\uparrow(\vec{r})$ affects the mode occupations.

In the energy basis we have $u_i(\vec{r}) \propto |\psi_i(\vec{r})|^2$, where $\psi_i(\vec{r})$ are the eigenfunctions corresponding to the effective potential imposed by the cavity mirrors. The frequency dependent proportionality factor can be absorbed by the Einstein coefficients to form the absorption and emission rates, $R^i_\uparrow$ and $R^i_\downarrow$. This leads to a final form of the system of equations, which matches Eqs. (3.15), (3.16), derived from a microscopic theory.

3.4 Mode selection

In the following discussion we will use the general term “Bose selected” for modes acquiring macroscopic occupation, which subsumes both equilibrium Bose condensation as well as non-equilibrium processes leading to a macroscopic occupation of bosonic modes [26, 27, 46, 47].

Setting the right-hand side of Eq. (3.15) to zero, it follows that a steady state population n_i is given by

$$n_i = \left(\frac{R^i_\uparrow}{R^i_\downarrow} \frac{(1 - G_i)}{G_i} - 1 + \frac{\kappa}{R^i_\downarrow \rho G_i} \right)^{-1}. \tag{3.24}$$

When a mode i becomes macroscopically occupied (“Bose selected”), the contribution of spontaneous emission to this macroscopic population n_i becomes negligible ($n_i + 1 \approx n_i$). This allows us to find a sharply defined threshold value G^{th}_i of the gain at which the “selection” happens. It is obtained by setting the term in the brackets to zero (corresponding to a divergent occupation). We get

$$G^{th}_i = \frac{R^i_\uparrow + \kappa/\rho}{R^i_\uparrow + R^i_\downarrow} = \frac{R^i_\uparrow / R^0_\uparrow + 1/\xi}{R^i_\uparrow / R^0_\uparrow + R^i_\downarrow / R^0_\uparrow}, \tag{3.25}$$

where we have isolated the thermalization parameter [19, 31]

$$\xi = R^0_\uparrow \rho/\kappa \tag{3.26}$$

as a dimensionless measure of the coupling between the photons and the dye relative to the cavity loss. For a sufficiently large density ρ, the collisions between the dye molecules and the solvent molecules are frequent enough that photons can thermalize via multiple absorptions and emissions within their cavity lifetime $1/\kappa$ [11, 48]. Therefore, the degree of thermalization increases with both ρ and $1/\kappa$. One of the requirements of an effective thermalization in the system is also that the absorption at the ground mode is not too low, making $R^0_\uparrow$ a reasonable choice in this definition. However, it is somewhat arbitrary and it does not affect the results, given that the same quantity is divided from the absorption and emission rates $R^i_{\uparrow,\downarrow}$ to obtain the dimensionless form of the rate equations used in the numerical calculations. Once a mode is selected, the gain G_i is clamped [9] at (or, more precisely, slightly below) the threshold value G_i^{th}. Namely, when increasing G_i further, n_i would diverge at $G_i = G_i^{th}$ and assume unphysical negative values for $G_i > G_i^{th}$.

Inserting the Kennard-Stepanov law (3.8), Eq. (3.25) can be written in the form

$$G_i^{th} = \frac{1 + R^0_\uparrow/(R^i_\uparrow \xi)}{1 + Ce^{-\beta(\varepsilon_i - \hbar\omega_{zpl})}}. \tag{3.27}$$

3.5 Equilibrium limit

In the case of equilibrium Bose-Einstein condensation, this “divergent” (macroscopic) occupation in the ground mode happens when the chemical potential approaches the value of ground mode energy. This locking of the chemical potential can be shown to be equivalent to the above defined clamping of the gain G_i in the limit $\xi \to \infty$ for the case of homogeneous excitation field $f(\vec{r}) = const. \equiv f$. Equation (3.24) then reduces to the Bose-Einstein distribution

$$n_i = \left(e^{\beta(\varepsilon_i - \mu)} - 1\right)^{-1}, \tag{3.28}$$

where we have used the Kennard-Stepanov law [Eq. (3.8)] and identified the chemical potential μ of the photon gas to be given by [42]

$$e^{\beta\mu} = Ce^{\beta\hbar\omega_{zpl}} f/(1-f), \tag{3.29}$$

as derived in Chapter 2. Here $f/(1-f)$ is a spatially homogeneous ratio of the number of excited and ground-state dye molecules. In the limit where the chemical potential approaches the ground-state energy, $\mu \to \varepsilon_0$ (onset of BEC), Eq. (3.29) becomes $Ce^{-\beta(\varepsilon_0 - \hbar\omega_{zpl})} = (1-f)/f$. It follows that $f = G_0^{th} = 1/(1 + Ce^{-\beta(\varepsilon_0 - \hbar\omega_{zpl})})$, which is exactly the selection threshold condition for the ground mode given by Eq. (3.25) when the photon cavity lifetime $1/\kappa \propto \xi \to \infty$. Therefore, in the equilibrium limit, which does not require pumping in order to stabilize the average photon number, the locking of the chemical potential is equivalent to the clamping of the gain.

Chapter 4

Homogeneously pumped photon gas

In this chapter, which is adapted from [32], we consider the case of a homogeneously pumped system, $P(\vec{r}) = const = P$ [1].

The equations of motion (3.15), (3.16) derived in Chapter 3 form a large system of coupled nonlinear differential equations. To obtain numerically the steady-state solution, we use the parameter values which correspond to the experiments of Refs. [10, 24, 30]. We choose a slightly anisotropic harmonic trap, as defined in Chapter 3, with $\Omega/2\pi = 4$ THz. As mentioned in Chapter 3, due to the large spacing between successive longitudinal modes, only one of these modes occupies the cavity at room temperature. That is, the energy spacing $\Delta\varepsilon = \hbar\tilde{c}\pi/D_0 \approx 3$ eV is much larger than the thermal energy $k_B T \approx 0.026$ eV. The ground-mode (cutoff) frequency is set to $\omega_c = \varepsilon_0/\hbar = 2\pi \cdot 515$ THz and the zero-phonon frequency (dashed vertical line in Fig. 4.1) is $\omega_{zpl}/2\pi = 555$ THz. From the measured absorption and fluorescence spectra of the Rhodamine 6G dye [19], we obtain the corresponding rates $R^i_{\uparrow,\downarrow}$ as fitted functions of the frequency ε_i/h [19, 49] using a cubic smoothing spline, as shown in Fig. 4.1. The values of the absorption and emission rates across the whole frequency range are determined by setting the absorption rate of the ground mode to $R^0_\uparrow/d^2 = 1$ kHz. The density of dye molecules is set to $\rho = 10^8/d^2$ and the thermalization parameter ξ lies between 0.01 and 100, where $\xi = 25$ corresponds to the mean experimental value of the photon loss rate $\kappa \approx 4$ GHz. The rate of spontaneous losses into non-cavity modes is set to $\Gamma = 0.2$ GHz.

We kept 28 modes (corresponding to 7 energy levels) in our numerical calculations. The value of the frequency spacing Ω between the modes was chosen large enough, while also achievable experimentally [30], so that increasing the number of modes considered

---

[1] The pump can also be modeled as a very wide Gaussian beam, to more accurately correspond to the experiment. This introduces only minor quantitative changes into the work presented here, without affecting any of the qualitative results.

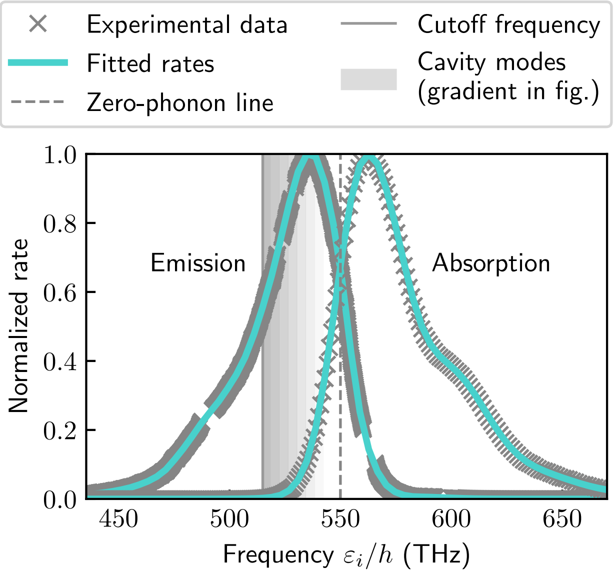

FIGURE 4.1: Fitted absorption and emission rates (solid lines) vs. frequency ε_i/h. The rates are fitted to experimental data (crosses) [19, 49] using a cubic smoothing spline. The frequency range of the relevant cavity modes is indicated by the shaded gray area with a sharp cutoff at $\omega_c = \varepsilon_0/\hbar$.

would not produce a significant effect on the results. That is, any additional modes would remain unselected across the whole pump-rate range and would not affect the transition thresholds of the selected modes. We used the LSODA algorithm and set a sufficiently large time interval to achieve convergence to a steady state for the range of parameters used. The initial condition was set to a zero mode-population vector for the lowest value in a range of pump rates P, and adapted to the current solution at each successive value of P. We also solved the steady-state equation directly via a root finding algorithm to confirm that both methods produce exactly the same results.

4.1 Threshold pump rate

The general condition for the selection threshold pump rate P_i^{th} of mode i can be obtained by inserting Eq. (3.16) into the definition of the gain (3.17) and setting it equal to G_i^{th}. We get [31]

$$G_i^{th} = \int d\vec{r}\, |\psi_i(\vec{r})|^2 \, \frac{P + \sum_{j\in S} R_\uparrow^j \, |\psi_j(\vec{r})|^2 \, n_j}{\Gamma + P + \sum_{j\in S} (R_\uparrow^j + R_\downarrow^j) \, |\psi_j(\vec{r})|^2 \, n_j}, \tag{4.1}$$

where the sums in the integrand are over all of the modes which have already been Bose-selected at lower pump rates. Again, the sharpness of transitions allows us to omit the contributions of spontaneous emission to the mean occupations, which are negligible once a mode is selected.

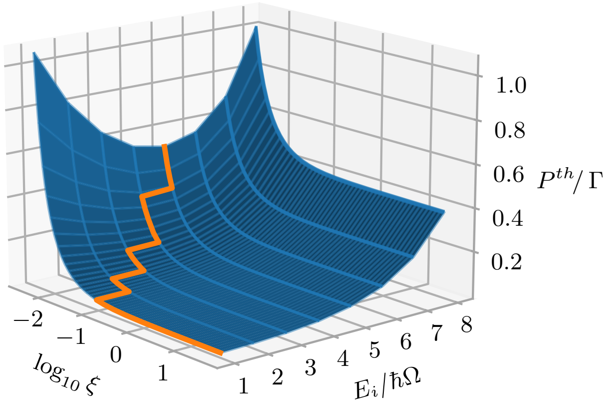

FIGURE 4.2: Threshold pump rate P_{th} of the first selection as a function of the thermalization parameter ξ and the energy E_i of the modes.

This equation would allow us, in principle, to iteratively determine each selected mode and the corresponding threshold pump rate, if the populations of all the already selected modes are known as a function of the pump rate P. Namely, at each value of ξ, the selected mode is the one for which the Eq. (4.1) holds for the lowest value of P. However, an analytic expression can only be obtained for the first selection. Here, the approximate value of the threshold P_i^{th} can be obtained by setting all n_j to zero (i.e. neglecting the coupling to the still weakly occupied photonic modes). Equation (4.1) then reduces to

$$G_i^{th} = \frac{P}{\Gamma + P}. \tag{4.2}$$

Solving this equation for P and inserting the condition (3.25), we get the first-selection threshold pump rate P_i^{th} as a function of the thermalization parameter ξ

$$P_i^{th} = \frac{G_i^{th}}{1 - G_i^{th}}\Gamma = \frac{R_\uparrow^i + R_\uparrow^0/\xi}{R_\downarrow^i - R_\uparrow^0/\xi}\,\Gamma. \tag{4.3}$$

It follows that the first-selected mode is the one with the lowest threshold gain $G_i^{th}(\xi)$. In Fig. 4.2 the threshold pump rate P_i^{th} is shown as a function of ξ and the mode energy E_i (blue surface). The orange line on this surface follows the minimal P_i^{th} at each value of ξ. We see that only for very small values of the thermalization parameter, $\xi \lesssim 0.1$, this is not the ground mode. This follows from Eq. (3.25) when taking into account the shapes of the absorption and emission spectra (see Fig. 4.1). In particular, by looking at the second equation we see that the ξ-independent denominator always favors the ground mode which has the largest Boltzmann factor, whereas the nominator contains the relative absorption rate of mode i, $R_\uparrow^i/R_\uparrow^0$, modulated by the thermalization parameter. When the latter is sufficiently large, $\xi \gtrsim 0.1$, this term becomes negligible compared to 1, and the selected mode is determined solely by the ground-mode favoring Boltzmann factor. On the

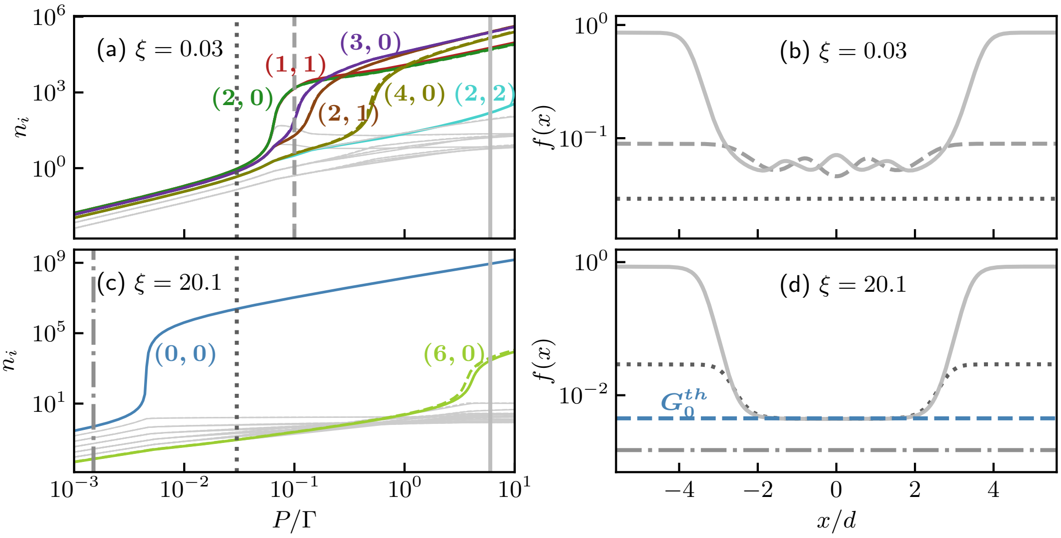

FIGURE 4.3: The left panel shows the mode populations n_i as functions of pump rate P for two values of the thermalization parameter, $\xi = 0.03$ (a) and $\xi = 20.1$ (c). Only one of the modes in an almost identically behaving symmetric pair is labeled. The right panel, (b) and (d), shows the corresponding spatial distributions of excited dye molecules $f(x)$ for the chosen values of P (vertical lines in the left panel).

other hand, in the high loss regime, $\xi \lesssim 0.1$, excited modes with higher relative absorption rate can “win out", i.e. have the smallest threshold gain.

4.2 Tuning the photon cavity lifetime and mode competition

Let us now discuss how the selection of modes is influenced by the thermalisation parameter ξ, or equivalently the photon cavity lifetime $1/\kappa$. Numerically obtained photon mode populations as functions of the pump rate are shown in Fig. 4.3 for two values of the thermalization parameter ξ. The colors correspond to the modes as shown in Fig. 3.3 and only modes with varying shapes are shown with different colors, e.g. symmetric pairs like (2,1) and (1,2) are depicted with the same color (brown), but a different linestyle (solid vs. dashed). These same colors are used consistently in all the figures of this chapter. As expected from Fig. 4.2, for the low value $\xi = 0.03$ (Fig. 4.3a), multiple quasi-degenerate excited modes (2,0), (0,2) and (1,1), colored green and red, respectively, are selected at practically identical threshold pump rate. This is followed by further selection of modes with higher energy, while the ground mode (0,0) remains unselected.

When ξ is sufficiently large, as shown in Fig. 4.3c, the ground mode is the first one to get selected at a much lower value of P. However, as P is increased further, eventually also modes (6,0) and (0,6) get selected, as opposed to the energetically favorable selection of the

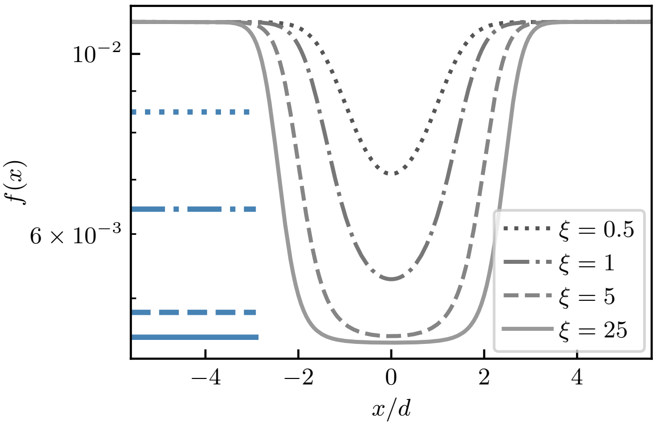

FIGURE 4.4: Spatial distributions of excited dye molecules $f(x)$ close above the first selection threshold P^{th} for 4 values of the thermalization parameter ξ. The corresponding threshold gain G^{th} is marked by a horizontal blue line of the same style.

first excited modes (1,0) and (0,1), which according to Eq. (3.25) possess a lower threshold gain G_i^{th}.

In order to explain this, we plot the fraction of excited dye molecules $f(x) \equiv f(x, 0)$ in Fig. 4.3d for three chosen values of P (indicated by vertical lines of the same style in the left panel). We see that once P is increased above the first selection threshold, the shape of $f(x)$ reflects the clamping of the gain in the central region, which overlaps with the selected ground-state mode. This clamping in the center of the trap then suppresses the selection of further low-energy modes, whose wave functions have a large weight in the trap center. This mechanism of mode repulsion explains why after the ground mode, the next modes to be selected posses six excitation quanta. Likewise, Fig. 4.3b shows that after the first selection $f(x)$ reflects the shape of the selected excited modes for the scenario of Fig. 4.3a.

To see more clearly how the shape of $f(x)$ and with that the mode competition changes with ξ, we plot its value at $P = 0.02$ for 4 values of ξ (Fig. 4.4). This pump rate is slightly above the first selection threshold P^{th} and only the ground mode is selected in each case. It follows from Eqs. (3.25) and (4.3) that a higher value of ξ lowers the first selection threshold and the corresponding gain gets clamped at a lower value G^{th}, indicated by horizontal blue lines for each ξ in Fig. 4.4. We see that with increase of ξ the excited dye molecules are clamped both at a lower value and in a wider spatial region, therefore becoming progressively more inaccessible to modes close in energy to the ground mode. In other words, when the gain is clamped at lower values, not enough molecules can be excited in the region of overlap between the ground mode and following excited modes. We can say that successive modes (those with largest overlap) “compete" for gain in the same spatial domain and block each other from being selected together in the regime of higher P.

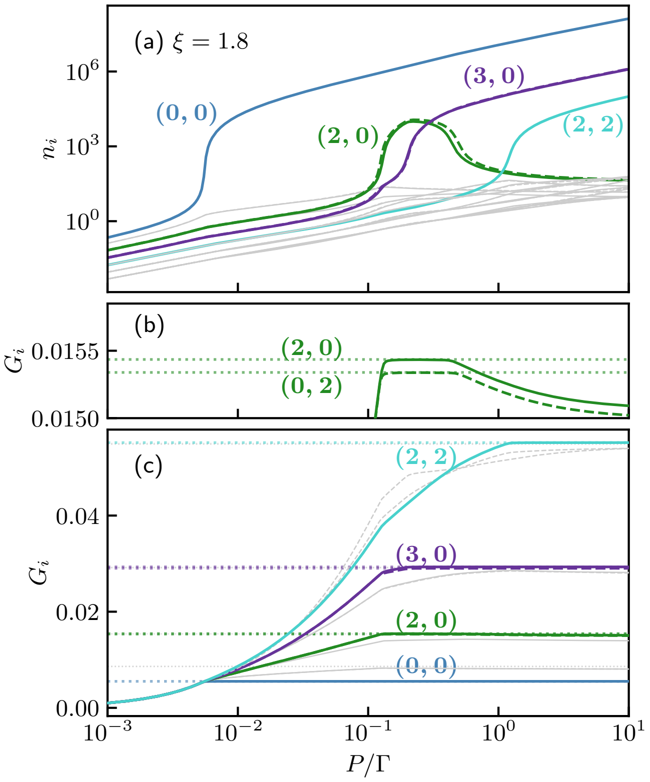

FIGURE 4.5: Population n_i (a) and gain G_i (c) of modes i vs. pump rate P for $\xi = 1.8$. Only one of the modes in an almost identically behaving symmetric pair is labeled. Dotted horizontal lines indicate threshold values G_i^{th} to which the gain is clamped at selection. The middle panel (b) shows the zoomed-in gain of modes (2,0) and (0,2), which are deselected when the clamped gain starts to drop below $G_{(2,0)}^{th}$ and $G_{(0,2)}^{th}$, respectively.

When the thermalization parameter is increased even further to $\xi = 20.1$ (Fig. 4.3d) $f(x)$ is locked to an even lower threshold value of the gain G_0^{th} (dashed blue line) in an even wider middle region. In this way, when increasing ξ, a quasi-equilibrium steady state is approached, where the gain clamping is equivalent to locking of the chemical potential. The fact that $f(x)$ is free to increase with the pump power in the outer spatial region until gain saturation is reached (no more dye molecules available to excite) reflects the non-equilibrium nature of the system.

Another observation that we can make from Fig. 4.3 is that, while the modes (6,0) and (0,6) are selected in high P regime, all the other modes with the *same* energy (like (3,3), (4,2), (5,1) etc.) remain unselected due to the key influence of the dye excitation profile on the behavior of modes. This is another indicator of the non-equilibrium nature of this state (even though at lower P where only (0,0) is selected, this state can hardly be distinguished from the equilibrium photon BEC (of a finite system), as will be discussed below in more detail).

In Fig. 4.5, at an intermediate value of the thermalization parameter $\xi = 1.8$, we can also observe the phenomenon of "deselection". Namely, we can see that the green-colored mode pair (2,0) and (0,2) gets deselected, as the purple-colored one, (3,0) and (0,3) is selected (Fig. 4.5a) [henceforth for brevity, mode pairs $\{(i,j),\ (j,i),\ i \neq j\}$ are denoted simply as "mode pair (i,j)"]. Fig. 4.5(c) depicts the corresponding gain G_i of each mode (solid curves) as a function of the pump rate. The threshold values of the gain G_i^{th} are shown as the dashed horizontal lines. One can see that each mode selection [Fig. 4.5(a)] is accompanied by gain clamping [Fig. 4.5(c)]. Decondensation of photonic modes was already discussed in Ref. [31] and a similar effect was predicted in a system of driven-dissipative polariton condensate [50]. This is another manifestation of the above-mentioned competition between successive modes which have a large spatial overlap. It happens when not enough dye molecules are pumped to their excited states in the combined region of mode density for both mode pairs to stay selected. Once, after the ground mode, the mode pair (2,0) is selected, $f(\vec{r})$ can only increase in a very restricted way, such that it stays clamped close to both $G_{(0,0)}$ and $G_{(2,0)}$ (dotted lines in Fig. 4.5c). This restriction still allows for the selection of the mode pair (3,0). However, the more particles this third selected pair acquires, the more attractive it becomes for further photons due to bosonic enhancement (i.e. stimulated emission). This non-linear effect leads to a competition with the energetically slightly favored (2,0) modes, which eventually causes the decondensation of the latter. This is accompanied by the "declamping" of its gain, which is better visible in Fig. 4.5b showing the zoom-in around $G_{(2,0)}^{th}$.

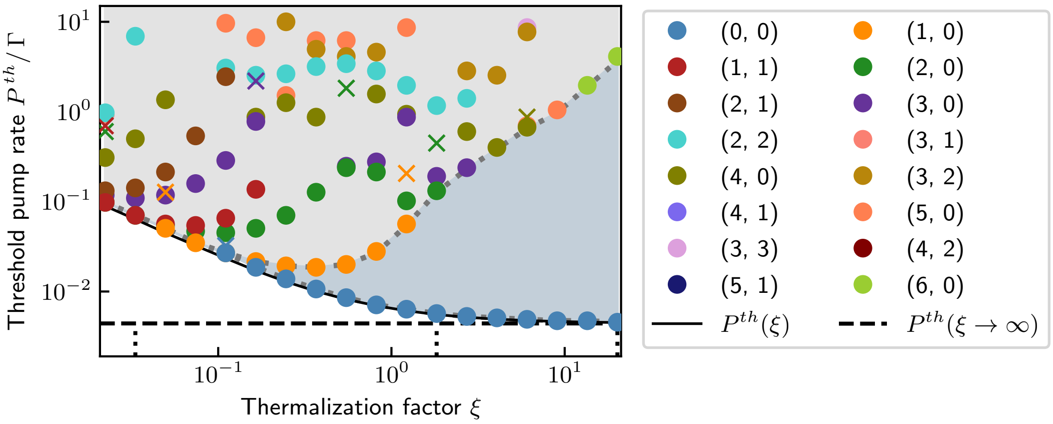

FIGURE 4.6: Phase diagram showing three main regions. The white region has no selected modes, only the ground mode is selected in the blue region, and there are multiple selections in the gray one. Colored dots (crosses) are numerical points indicating selections (deselections) of the corresponding modes. The dotted line is the lower (upper) phase boundary, interpolating between the points of first (second) selection. The pump rate at which the two phase boundaries meet is the minimal P for which the ground mode is selected. Below this pump rate ("lasing phase"), the phase boundaries are indistinguishable, because multiple quasi-degenerate higher energy modes are selected at almost exactly the same P. The analytical result for the first selection threshold (Eq. (4.3)), is shown with a solid black line. In the high ξ regime, this phase boundary approaches the dashed horizontal line, showing the high thermalization limit of Eq. (4.3) $P^{th}(\xi \to \infty)$. The three dotted vertical lines mark the cuts through the phase diagram shown in Fig 4.3 and Fig 4.5.

4.3 Phase diagram

After having discussed the role of mode competition for the selection of excited cavity modes, let us now compute the phase diagram of the system in the parameter plane spanned by the pump rate and the thermalization parameter. Figure 4.6 shows a phase diagram where the various phases are characterized by which modes are selected. There are no macroscopically occupied modes in the white region. Only the ground mode is selected in the blue region, whereas in the gray one, there are multiple selected modes. Colored dots (crosses) are numerical points indicating selections (deselections) of the corresponding modes. The lower and upper phase boundaries (dotted lines) are obtained by interpolating between the points of first (second) selection. Below the value of ξ at which both boundaries meet, the mode which become selected first is not the ground state anymore. Below this point, the two phase boundaries are indistinguishable, because multiple quasi-degenerate higher energy modes are selected at almost exactly the same P. The solid black line indicates the analytical result for the first selection threshold, given by Eq. (4.3) and shown with the orange line in Fig. 4.2. It closely matches the numerical result, especially in the high ξ regime, where it approaches the high thermalization limit of Eq. (4.3) $P^{th}(\xi \to \infty)/\Gamma = R^0_\uparrow/R^0_\downarrow$ (dashed horizontal line).

We note that our phase diagram differs from the one obtained in Ref. [31]. Namely, in agreement with the analytical prediction (4.3), we find that the threshold pump rate for the first selection process decreases as a function of the thermalization parameter, while it increases in Ref [31].

In the regime of low ξ, where the photon cavity lifetime is too short for photons to effectively thermalize, there are multiple high energy modes selected closely together instead of the ground mode, and these transitions to macroscopic occupation represent the limit where the operation of the system would typically be considered as that of a laser. Given that drive and thermalization are both present in this system, Bose condensation cannot be sharply distinguished from lasing. Nevertheless, this phase diagram still clearly shows the trend of going from the lasing limit towards the BEC limit as the thermalization parameter is ramped up.

The second phase boundary separates the blue region with only the ground state selected from the gray one, where also excited modes have acquired a large occupation. With increasing ξ, the separation between the P_0^{th} of the ground mode selection and the P_j^{th} of the next selected mode j increases together with its energy E_j, due to mode competition explained above. In this way, a limit of quasi-equilibrium photon BEC is approached for large ξ and pump powers well below the second selection threshold.

To support this claim, in Fig. 4.7 we compare the Bose-Einstein (BE) distribution $\ln(1 + 1/n_i) = \beta\varepsilon_i - \mu$ (straight orange line) with the distribution of numerically obtained mode

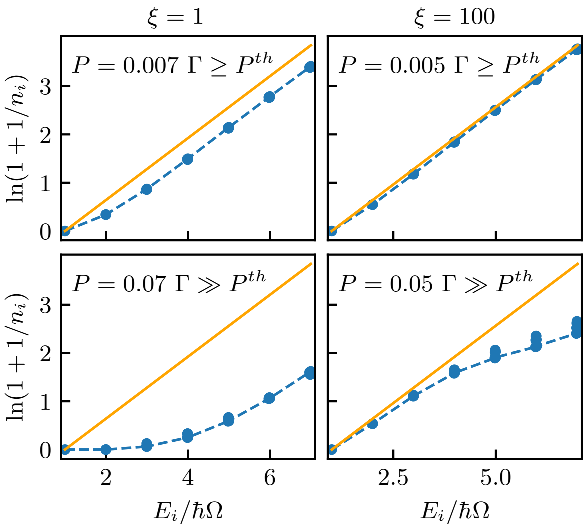

FIGURE 4.7: Numerical mode population n_i (blue dots) vs mode energy E_i compared to the thermal distribution (orange straight line) below, close above and far above the first selection threshold P^{th} when $\xi = 1 \Rightarrow P^{th} = 0.0065\,\Gamma$ (left panels) and $\xi = 100 \Rightarrow P^{th} = 0.0044\,\Gamma$ (right panels).

populations n_i (blue dots), for P close and far above the first selection threshold P^{th}. Left panel corresponds to $\xi = 1$, and the right one to $\xi = 100$, for which only the ground mode is selected. As expected, for higher ξ, the match between the numerical points and the thermal distribution is better, particularly when P is only slightly above the threshold, $P \gtrsim P^{th}$. Here the small deviations are only due the fact that the absorption and emission rates fitted to measured data (Fig. 4.1) do not satisfy the Kennard-Stepanov relation (Eq. (3.8)) exactly, but only to a very good approximation. As P is raised significantly above P^{th}, the numerically obtained populations start to deviate from the BE distribution, particularly those of higher modes. This is expected, even though at the very high value of ξ, no other mode is selected at $P \gg P^{th}$ except the ground mode. The reason for this is that outside of the increasingly wide central region of the trap where the gain is clamped, $f(x)$ can still increase with P. Therefore, the occupation of modes with a high density there (higher energy modes) can increase as well, moving away from the thermal distribution.

4.4 Tuning the cutoff frequency

Let us finally discuss how the physics of the mode selection changes, when considering a variation of the cutoff frequency ω_c (or equivalently, the detuning from the zero-phonon line). The cutoff frequency corresponds to the ground-mode energy and can be tuned experimentally by varying the longitudinal frequency ω_L via the cavity length. It determines the absorption and emission rates, thus affecting also the degree of thermalization. This has been studied experimentally for the case of a continuous wave (CW) [10] and pulsed laser pump [24], as well as in theoretical work [20].

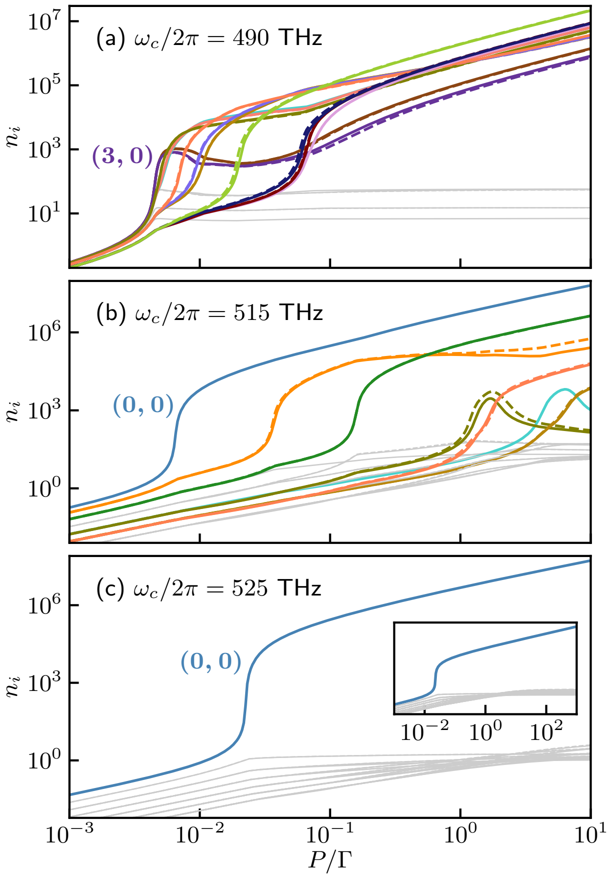

FIGURE 4.8: Population n_i of modes i vs. pump rate P for $\xi = 1$. The cutoff frequency is $\omega_c/2\pi = 490$ THz (a), $\omega_c/2\pi = 515$ THz (b) and $\omega_c/2\pi = 525$ THz (c). The inset of panel (c) contains the same result extended to high P regime, showing that only the ground mode is selected before the gain is saturated.

In Fig. 4.8 we show the numerical results for the photon populations n_i for three different values of the cutoff frequency, while keeping the thermalization parameter fixed at $\xi = 1$. Changing the cutoff frequency, i.e. the ground-mode energy, corresponds to shifting the frequency range of cavity modes (sketched by the gray shaded area in Fig. 4.1) to the left or right. This affects the threshold gain G_i^{th} of each mode (Eq. (3.25)). For sufficiently low cutoff frequency $\omega_c/2\pi = 490$ THz (Fig. 4.8a), the absorption and emission rates no longer satisfy the Kennard-Stepanov law. Instead of the ground mode, now an excited mode pair (3,0) has the lowest value of G_i^{th} and it is selected first, closely followed by additional excited modes, while the ground mode remains unselected. In the case of higher $\omega_c/2\pi = 515$ THz (same value used for all the rest of our results), the ground mode is selected first, followed by the selection of several excited modes, as seen in Fig. 4.8b.

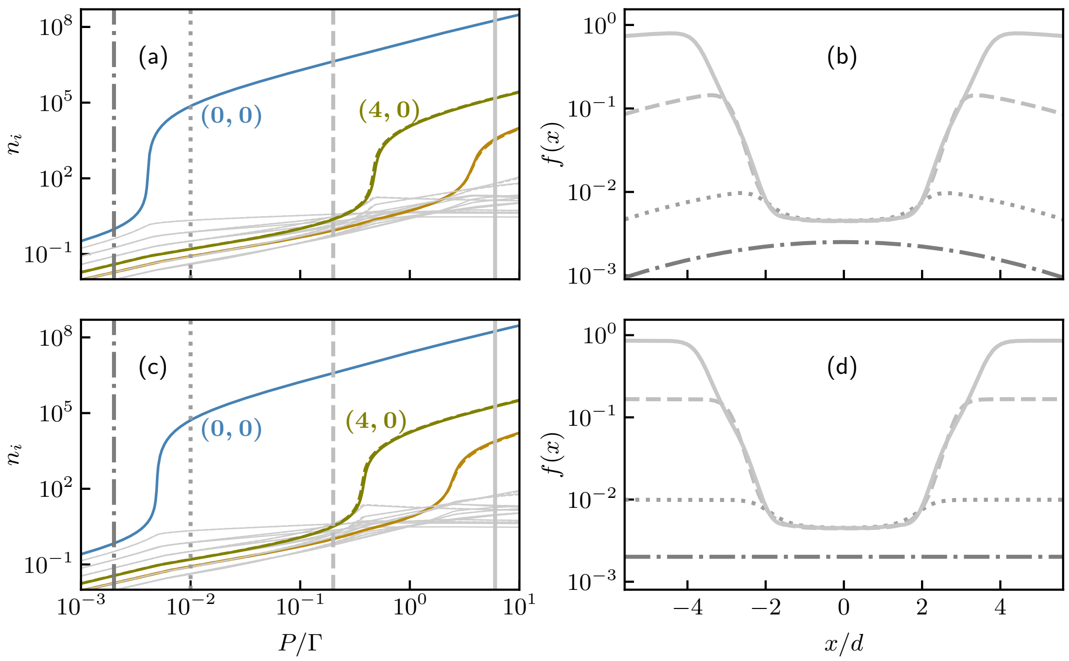

FIGURE 4.9: The upper panels correspond to the case of a wide Gaussian pump profile and show the mode populations n_i vs. P (a) and $f(x)$ for the chosen values of P (b), indicated by the vertical lines in the left panel. The same quantities are shown in the lower panels (c, d) for the case of a constant pump profile. In both cases the thermalization parameter is $\xi = 4$.

Compared to Fig. 4.8a, the threshold pump rate P^{th} of the first selection has increased. When the cutoff frequency is shifted even further to $\omega_c/2\pi = 525$ THz, only the ground mode is selected before the gain is saturated (Fig. 4.8c) and no further selections can occur. This is shown in the inset, where the P axis is extended by 2 orders of magnitude. In this case the Kennard-Stepanov law still holds, but the corresponding P^{th} and G^{th} are now the highest. It should be pointed out that in the actual experiment, as the cutoff frequency is varied, the photon cavity lifetime also varies significantly [24]. In the case of here chosen ω_c values, this means that ξ should increase with ω_c [2]. However, this would only enhance the effect of increase in photon thermalization, observed from (a) to (c) panel in Fig. 4.8.

We end this chapter by comparing the results obtained using a constant pump rate (as used throughout this chapter) with the ones produced when the pump has a wide Gaussian profile, corresponding to the experiments [11]. More precisely, it has the form $p(\vec{r}) = P\, g_{\mu,\sigma}(\vec{r})$, where $g_{\mu,\sigma}(\vec{r})$ is a normalized 2D off-centered Gaussian with standard deviation $\sigma = 4\, d$ and mean $\mu = (0, 0)$. In Fig. 4.9 we show the steady-state mode populations n_i as functions of P on the left, and the corresponding $f(x)$ for the chosen values of P on the right, marked by the vertical lines in the left panels. The thermalization parameter is set to $\xi = 4$. The case of a wide Gaussian pump profile is shown in the upper panels (a, b), while the lower ones show the case of a constant pump rate for comparison. We can see that only minor quantitative differences are present. Namely, the threshold values of P are slightly shifted and $f(x)$ reflects the Gaussian pump profile in the outer region (upper panel), while the shape in the middle, reflecting the clamping of the gain, is almost identical in both cases.

---

[2] Alternatively, we could consider (a), (b) and (c) to correspond to different cavities, which have the same photon loss rate κ at the given cutoff frequencies.

Chapter 5

Off-centered pump beam

This chapter, as well as the following one, is adapted from [33]. Here we explore an alternative non-equilibrium scenario, where the interplay between driving and thermalization is controlled by an *off-centered* and (relatively) narrow pump beam. This gives rise to a robust engineering and the control of multi-mode emission. We find that the system undergoes two pump-power driven non-equilibrium phase transitions. First, the system starts to lase in an excited mode, which is directly determined by the position of the pump spot. When the pump power is increased further, the spatial redistribution of pump power mediated by this lasing mode then triggers a second transition, where thermalization leads to the additional formation of an equilibrium-like Bose condensate in the ground mode. In a system where both drive and thermalization are present, a sharp distinction between lasing and Bose condensation is, strictly speaking, no longer possible. Nevertheless, the characterizations of the first transition as lasing and the second as condensation provides a useful way to mark the mechanisms (selective pumping vs. thermalization) that are mainly responsible for the mode selection. The fact that the lasing mode can be selected by adjusting the pump spot, while the second transition always corresponds to the onset of ground-state condensation, makes this mechanism of lasing-assisted Bose condensation a promising tool for engineering systems with robust and tunable two-mode emission.

The spatially varying pump rate has the form $p(\vec{r}) = P\, g_{\mu,\sigma}(\vec{r})$, where $g_{\mu,\sigma}(\vec{r})$ is a normalized 2D off-centered Gaussian with standard deviation σ and mean $\mu\vec{e}_x$. In the equation of motion (3.16), this $p(\vec{r})$ now replaces the previously constant pump rate P. We compute the steady state of the system using the same parameter values listed in the Chapter 4, with the exception of the frequency spacing, which is now set to $\Omega/2\pi = 3$ THz (as opposed to the previously used $\Omega/2\pi = 4$ THz) [1]. The Gaussian pump spot of width $\sigma = 0.4\ d$ is shifted away from the trap center by $\mu = 3.2\ d$, so that it has essentially no overlap with

---

[1] This value was chosen for computational reasons and it was checked that increasing the number of modes does not produce any significant changes in the results. Namely, those additional modes remain unselected for the whole range of pump rates, while the selected modes and the associated threshold values stay the same.

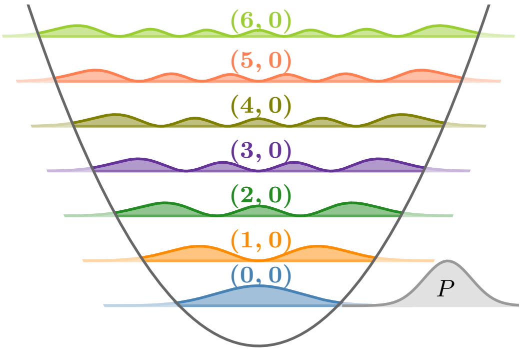

FIGURE 5.1: Off-centered Gaussian pump spot (P) and photon modes $|\psi_{n_x,n_y}(x)|^2$ projected onto the x axis. For simplicity, only modes $(n_x, 0)$, with nodes only along x direction, are shown.

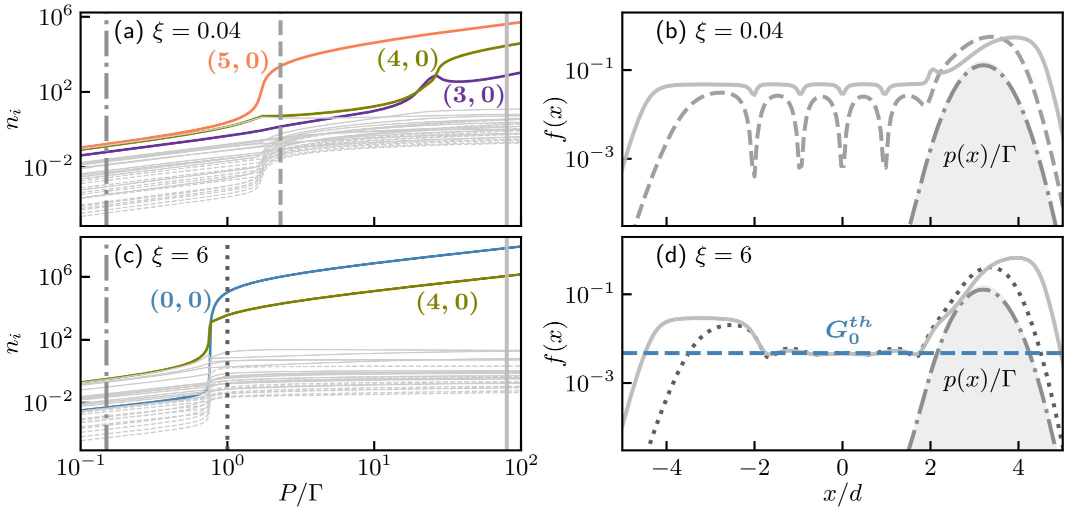

FIGURE 5.2: Population n_i of mode i vs. pump rate P for $\xi = 0.04$ (a) and $\xi = 6$ (c). Spatial distributions $f(x)$ of excited dye molecules along the x-axis (b, d) is shown for $\xi = 0.04, 6$ at those P marked by the corresponding vertical lines in (a, c), respectively. The shaded area represents $p(x)/\Gamma$. The threshold gain of the ground mode G_0^{th} is indicated by the dashed blue line.

the ground mode [see Fig. 5.1]. In this way, the competition between driving and thermalization is enhanced. A similar off-centered pump has already been realized experimentally to study the transient relaxation dynamics following a short pump pulse [24]. In contrast, we are interested in the steady state of the continuously pumped system.

5.1 Non-equilibrium steady state and lasing assisted ground-state condensate

Numerically obtained mode populations for $\xi = 0.04$ and $\xi = 6$ are shown in Figs. 5.2(a) and (b), respectively. The colors correspond to the modes as shown in Fig. 5.1. In the case of the lower value of ξ, a high-energy mode (5,0) (orange), which has a relatively large overlap with the pump spot, is selected first, followed by further selections of modes (3,0) and (4,0) at higher values of P. The ground mode remains unselected in the whole pump-rate range. At $P > 100\,\Gamma$ (i.e., above the largest P shown in Fig. 5.2), gain saturation has already been reached and no further selections can occur. When ξ is sufficiently high (b), the selection of the ground mode (blue), which is favored via the thermalization process, is triggered by the selection of mode (4,0) (green).

In order to understand, which mode becomes selected first, let us approximate the distribution of excited dye molecules in the steady state below the first threshold by $f(\vec{r}) \approx p(\vec{r})/(p(\vec{r}) + \Gamma) \approx p(\vec{r})/\Gamma$. Here the first expression is obtained from Eq. (3.16) by neglecting the coupling to the still weakly occupied photonic modes. Inserting this expression into the threshold gain given by Eq. (3.25), we get the following condition for the threshold pump rate of mode i

$$P_i^{th} = \frac{G_i^{th}}{G_i[g_{\mu,\sigma}(\vec{r})]}, \tag{5.1}$$

where $G_i[g_{\mu,\sigma}(\vec{r})] = \int |\psi_i(\vec{r})|^2 g_{\mu,\sigma}(\vec{r})\, d\vec{r}$ is the overlap of mode i with the pump profile. The selected mode i is the one with the lowest value of P_i^{th}. We see that there are two competing effects here. While the denominator favors modes having a large overlap with the pump spot (i.e. excited modes), the numerator favors modes with low energy. For a narrow pump spot with $\sigma/d \lesssim 1$, as considered here, we expect the former effect to be the dominant one. Figure 5.3 shows the threshold pump rate P_i^{th} of the first selection as a function of the pump spot position μ. Results from Eq. (5.1) (solid curve) match the exact values obtained numerically (dots) very well. The colors and the labels (n_x, n_y) indicate which mode is selected first; it changes at the vertical dotted lines. The colored bars at the bottom, in turn indicate the mode with the largest overlap with the pump spot. We can see that the impact of the nominator in Eq. (5.1) is to slightly shift the dotted lines with respect to the corresponding colored bars. However, as expected, energetics plays a minor role in the selection of the first mode compared to its overlap with the pump spot. For the value $\mu = 3.2\ d$, which was used for the simulations shown in Figs. 5.1 and 5.2 (arrow in Fig. 5.3), the selected mode is $(4, 0)$, which has only slightly lower $G_i[g_{\mu,\sigma}(\vec{r})]$ then the mode $(6, 0)$. Therefore, we will refer to the first selection as simply “lasing”, since (for $\mu \gtrsim d$) an excited mode is selected predominantly as a consequence of its large overlap with the pump spot, while the impact of thermalization is very small.

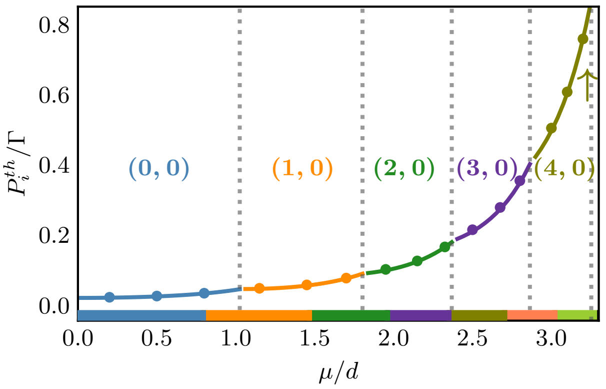

FIGURE 5.3: Threshold pump rate P_i^{th} for the first selection [Eq. (5.1)] vs. pump-spot position μ for $\xi = 6$. The different colors and labels (n_x, n_y), separated by dotted vertical lines, indicate which mode is selected. The dots are obtained numerically form the full rate equations. The colored bars at the bottom indicate the mode with the largest overlap with the pump profile $G_i[g_{\mu,\sigma}(\vec{r})]$ and the arrow points to the case shown in Fig. 5.2(c, d)

Once the system starts to lase in an excited mode, this mode will create excited dye molecules in an extended region in space, much larger than the narrow off-centered pump spot. This can be seen in Fig. 5.2(b, d) showing the spatial distribution $f(x)$ of excited dye molecules along the axis of the pump spot displacement (x-axis). The different linestyles correspond to the pump rates indicated by the vertical lines of the same style in Fig. 5.2(a, c). As mentioned previously, below the first threshold there are no selected modes and $f(x) \approx p(x)/\Gamma$, as can be seen from the perfect match between the dashed line and the shaded area denoting $p(x)/\Gamma$. The dotted curve, which shows $f(x)$ just above the lasing transition, has the additional structure corresponding to the first selected mode. This lasing assisted redistribution of pump-power can then trigger the selection of a second mode. For a sufficiently large thermalization parameter (which lowers the threshold gain G_0^{th} [Eq. (3.25)]), this mode is *always* found to be the ground state, which is favored via thermalization with the dye due to its lowest energy. Thus, in this respect, the second transition is akin to equilibrium Bose condensation and we call this effect lasing assisted ground-state condensation. In Fig. 5.2(d) we can also see that the threshold gain of the ground mode G_0^{th} (dashed blue line) roughly matches $f(x)$ in the center of the trap.

Although a range of ξ can be found for which only the ground mode and one excited mode are selected below dye saturation (a particular case is shown in Fig. 5.2(c, d)), there can be additional selections outside of this ξ range. This is shown in Fig. 5.4 where the mode populations are depicted for various ξ and μ values. In Fig. 5.5(a) we plot the mode populations vs. pump rate for a high value of ξ, while the corresponding spatial distribution of excited dye molecules along the x-axis is shown below [Fig. 5.5(b)] at values of P indicated by the corresponding vertical lines of the same style in the upper panel. We can see that there is an additional mode (5,0) selected before saturation is reached and that the

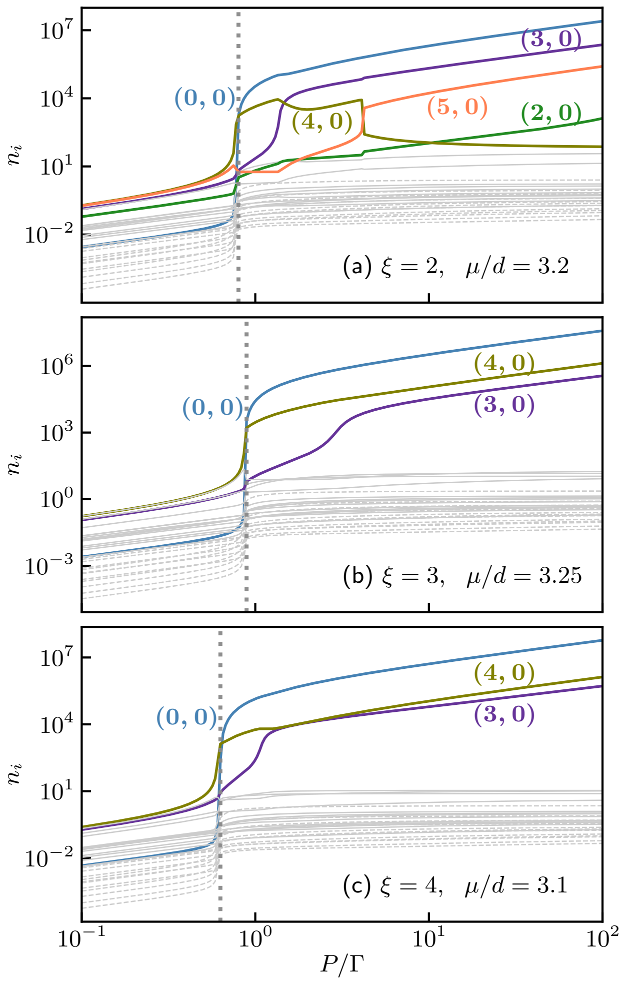

FIGURE 5.4: Population n_i of mode i vs. pump rate P for $\xi = 2,\ \mu/d = 3.2$ (a), $\xi = 3,\ \mu/d = 3.25$ (b) and $\xi = 4,\ \mu/d = 3.1$ (c). In each case, the threshold pump rate for the ground mode is marked by the dotted gray line.

chemical potential (proportional to G_0, as shown in Chapter 3) is approximately flat in the center of the trap for this relatively high value of ξ.

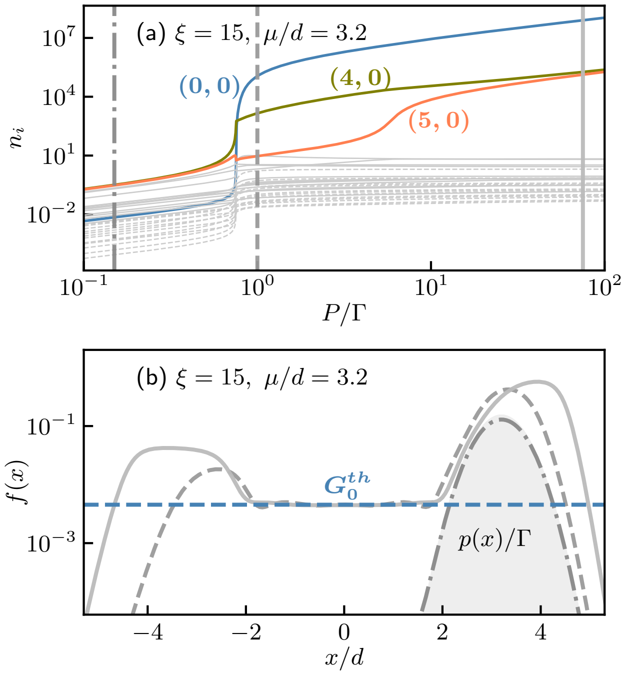

FIGURE 5.5: Population n_i of mode i vs. pump rate P (a) for $\xi = 15,\ \mu/d = 3.2$. Spatial distribution $f(x)$ of excited dye molecules along the x-axis (b) at those P marked by the corresponding vertical lines of the same style in (a). The shaded area represents $p(x)/\Gamma$. The threshold gain of the ground mode G_0^{th} is indicated by the dashed blue line.

Chapter 6

Structured cavity

In the previous chapter we have shown that the mode which is selected first can be accurately controlled via the position of the pump spot [Fig. 5.3] and that for sufficiently high thermalization parameter, the second transition always corresponds to the selection of the ground mode. Here we consider a structured potential (as introduced in Chapter 3). The idea is to explore the prospect of engineering systems with robust and tunable two-mode emission and to investigate how the effect can be controlled by shaping the transverse potential landscape in the cavity.

This can be done using recently developed experimental tools based on thermo-optic imprinting [30]. We consider a structured cavity imposing an asymmetric double-well potential for the photons, $V_{\mathrm{DW}}(x,y) = V_{HO}(x,y) + l\exp\left[-(x-\delta)^2/(2\varepsilon^2)\right]$. In the following we choose $l = 7.5\ \hbar\Omega$ and $\varepsilon = 1.0\ d$, while δ is used as a tuning parameter. Here Ω and d denote the angular frequency and the length associated with the harmonic oscillator potential $V_{HO}(x,y)$ given by the curved mirrors. We choose a pump beam with a Gaussian shape centered at the upper well minimum and sufficiently narrow (width $\sigma = 0.5\ d$) so that it has a negligibly small overlap with the modes localized in the lower well (see Fig. 6.1).

6.1 Controlled two-mode emission

In the upper panel of Fig. 6.1 we depict the potential and the corresponding photon modes for $\delta = 0.79\ d$ together with the pump profile $p(\vec{r})$ (gray), projected onto the x-axis. The modes shown in color are those that get selected. As shown in the lower panel of Fig. 6.1, for a slightly different value $\delta = 0.81\ d$, the lasing mode E_6 becomes delocalized between both wells, as a consequence of an inter-well resonance.

As already mentioned, this choice of trapping potential is motivated by recently developed technique for creating a structured transverse potential using thermo-optic imprinting

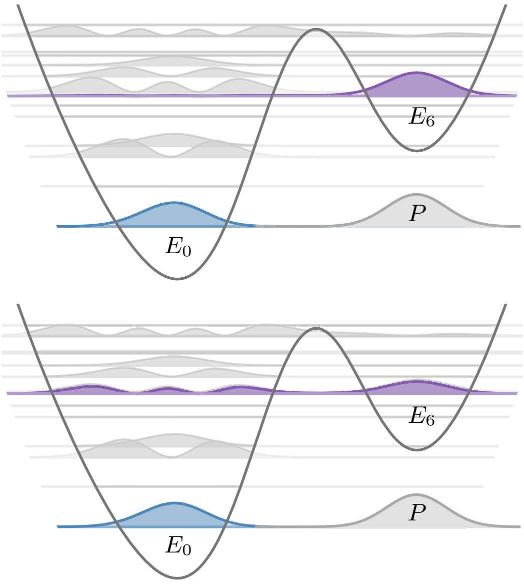

FIGURE 6.1: Upper panel: Double well potential and modes $|\psi_i(x)|^2$ for $\delta = 0.79\,d$ together with the pump spot (P), projected onto the x-axis. The modes shown in color (blue and purple) and labeled by their energy are those that get selected. Lower panel: For a slightly different value $\delta = 0.81\,d$, the lasing mode 6 becomes delocalized between both wells, as a consequence of an inter-well resonance.

[30]. Part of this experimental setup is shown schematically in Fig. 6.2. A thermosensitive polymer is added to the dye solution in a microcavity, so that variations of the refractive index are induced through irradiation with a heat-producing laser beam. This local heating increases the optical wavelength between the two mirrors. In the paraxial limit, this is equivalent to a locally decreased potential for the photon gas. In other words, in order to locally satisfy the boundary conditions imposed by the cavity, larger optical wavelength (corresponding to a smaller photon energy) is required.

In Fig. 6.3(a) we present the mode populations versus pump power for the potential shown in the upper panel of Fig. 6.1. The thermalization parameter is $\xi = 6$, the frequency spacing is set to $\Omega/2\pi = 4$ THz, while all the remaining parameters are the same as in previously discussed cases. Since, essentially, we are only pumping the upper well, mode E_6 (purple), having the lowest energy among those modes significantly overlapping with the pump spot, is selected first. The only other mode that gets selected at a higher P is the ground mode E_0 (blue). Thus, by modifying the cavity structure, we have isolated the effect of lasing-assisted ground-state condensation from the selection of further modes.

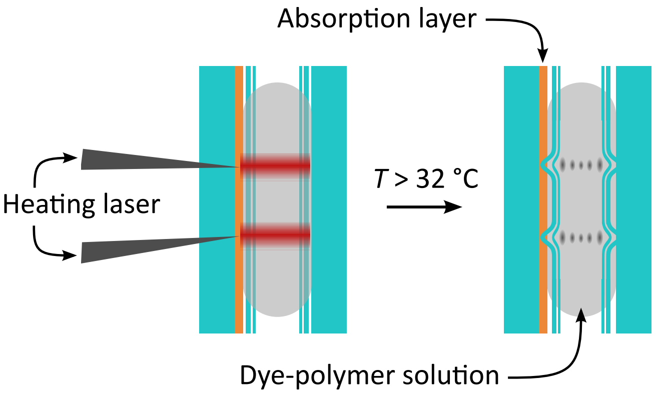
Absorption layer
Heating laser
$T > 32$ °C
Dye-polymer solution

FIGURE 6.2: Mechanism for creating a variable potential landscape for photons trapped in a microcavity [30]

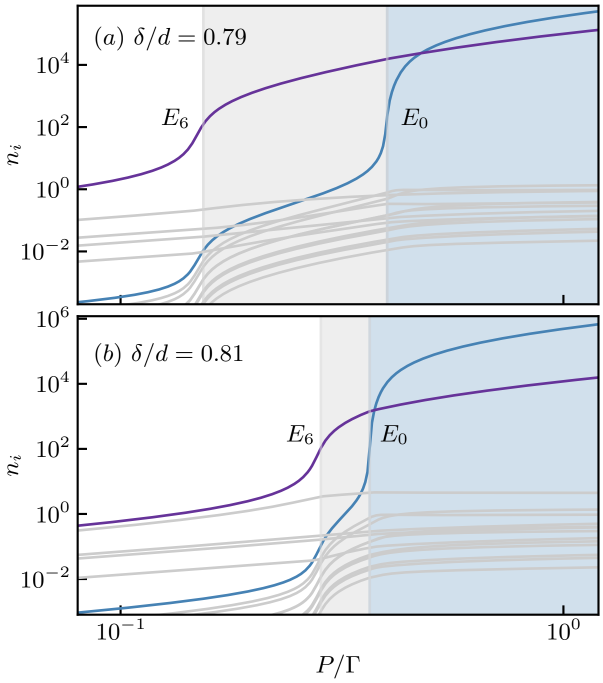

FIGURE 6.3: Mode populations n_i vs pump rate P for two slightly different values of δ. The grey area indicates a P range in which there is only lasing, while in the blue region the ground-state condensate is also present.

6.2 Effect of inter-well resonance

Figure 6.3(b) shows the mode populations for the slightly larger parameter $\delta = 0.81\ d$, corresponding to the double well potential shown in the lower panel of Fig. 6.1, which essentially looks the same as the one depicted in the upper panel. Note that this small parameter change leads to a large change in the separation between the first and the second threshold value. This strong sensitivity is caused by the delocalization of the lasing mode (purple) over both wells. This is a result of the resonant coupling to a mode in the left well. As a result, the lasing-assisted creation of excited dye molecules in the left well is strongly enhanced and the second threshold to ground-state condensation happens at much lower pump rates.

In Figure 6.4 we plot how the two threshold pump rates for lasing (gray curve) and ground-state condensation (blue curve) vary with δ, while the thermalization parameter is held fixed at $\xi = 1$. The two arrows indicate the values of δ shown in Fig. 6.3. One can clearly observe a sequence of resonances at which the second threshold is strongly reduced. The inset shows a zoom-in around the values of δ used in Fig. 6.3. Remarkably, these resonances can be used to control the second threshold value by orders of magnitude. The threshold for the first transition generally increases with ξ, but it also shows small peaks at the resonances, which are associated with a reduced overlap with the pump spot due to delocalization of the "lasing" mode. By engineering the transverse potential for the photons in the cavity, one can use this effect to widely tune the separation between the first and the second threshold.

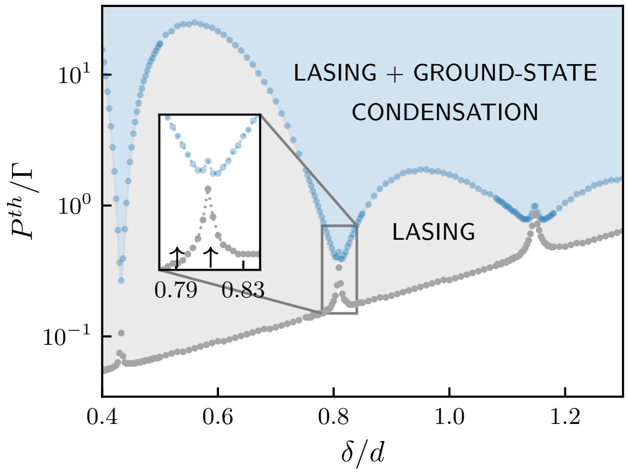

FIGURE 6.4: Phase diagram showing the resonance effect on the ground-state condensate. The two phase boundaries are numerically obtained threshold pump rates P^{th} for the lasing (gray) and the ground-state condensation (blue) as functions of δ. The arrows in the inset (zoom-in) correspond to the case shown in Figs. 6.1 and 6.3.

Chapter 7

Simplified model and analytic solutions

Having discussed in detail the numerically obtained solutions for the steady state of the system in different scenarios, which included varying the pump profile as well as the type of trapping potential, we now turn to a possibility of finding a simplified model which captures all the qualitative features discussed so far, while being analytically solvable.

We start with the last discussed case in the previous chapter - the double-well potential. We approximate the spatially dependent fraction of excited dye molecules as a constant $f(\vec{r}) = f_i$ in each of the two spatial "bins" ($i = 1, 2$) separated by a plane perpendicular to the x-axis and passing through the center of the potential barrier $(x_B, 0)$, which is the

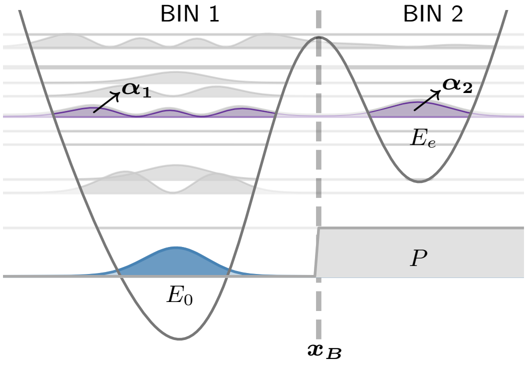

Figure 7.1: Simplified model: two modes, labeled E_0 and E_e are taken into account, as well as a spatially constant fraction of excited molecules in two regions separated by a plane (dashed line passing through the barrier center x_B), such that the ground mode can be taken as completely localized in the left one, whereas the excited mode can be distributed between both wells, with the respective fractions labeled by α_1 and α_2. Only the upper well is pumped with a constant rate P.

local maximum of the double-well potential (see Fig. 7.1). In other words, we use an ansatz

$$f(\vec{r}) = f_1\,\theta(x_B - x) + f_2\,\theta(x - x_B), \tag{7.1}$$

where $\theta(x)$ is the Heaviside step function. Only the second bin is pumped with a constant pump rate P, as shown in the figure. Within this simplification we also only keep two modes, the ground mode and one excited mode (labeled e) having the lowest energy of those with a significant intensity distribution in the pumped upper well. Since the spatial variance of the modes and the pump profile is neglected, the modes are only characterized by their energy and the fraction of their spatial distribution $\alpha_{1(2)}$ in each bin, respectively

$$\begin{aligned} \alpha_1 &= \int_{-\infty}^{x_B}\int_{-\infty}^{\infty} |\psi_i(\vec{r})|^2\,d\vec{r}, \\ \alpha_2 &= \int_{x_B}^{\infty}\int_{-\infty}^{\infty} |\psi_i(\vec{r})|^2\,d\vec{r}. \end{aligned} \tag{7.2}$$

Probability conservation (normalization of wavefunctions) requires that $\alpha_1 + \alpha_2 = 1$. For the ground mode, the probability to find it in the upper-well region is negligible and therefore $\alpha_1^0 = 1$ and $\alpha_2^0 = 0$. Likewise, the two contributions of the excited mode $\alpha_1^e \equiv \alpha_1$ and $\alpha_2^e \equiv \alpha_2$ will be approximately zero and one, respectively, except in the case of an inter-well resonance.

Except for reducing the full spatial resolution to only 2 bins and minimizing the number of modes which are taken into account, the resulting system of four equations with four unknowns is analogous to the rate equations (3.15), (3.16) and reads

$$\begin{aligned} \dot{n}_0 &= -\kappa n_0 + n_0\rho[f_1(R^0_\uparrow + R^0_\downarrow) - R^0_\uparrow] = 0, \\ \dot{n}_e &= -\kappa n_e + n_e\rho[(\alpha_1 f_1 + \alpha_2 f_2)(R^e_\uparrow + R^e_\downarrow) - R^e_\uparrow] = 0, \\ \dot{f}_1 &= -\Gamma f_1 + (1 - f_1)(R^0_\uparrow n_0/w_1 + R^e_\uparrow n_e\alpha_1/w_1) \\ &\quad - f_1(R^0_\downarrow n_0/w_1 + R^e_\downarrow n_e\alpha_1/w_1) = 0 \\ \dot{f}_2 = P(1 - f_2) - \Gamma f_2 &+ (1 - f_2)R^e_\uparrow n_e\alpha_2/w_2 - f_2 R^e_\downarrow n_e\alpha_2/w_2 = 0, \end{aligned} \tag{7.3}$$

where w_1 (w_2) is the area of the first (second) bin, respectively, while all the other symbols represent the same quantities as used previously. Here we have also neglected spontaneous emission in order to make the system analytically solvable.

We find that there are three steady-state solutions, each valid in a different pump-rate interval (labeled 1, 2 and 3 in Fig. 7.2). To solve the system (7.3), we first rewrite the second equation in the following form

$$\dot{n}_e = n_e\{\rho[G_e(R^e_\uparrow + R^e_\downarrow) - R^e_\uparrow] - \kappa\} = 0, \tag{7.4}$$

where $G_e = \alpha_1 f_1 + \alpha_2 f_2$ is introduced as the gain of mode e, analogously to the previously

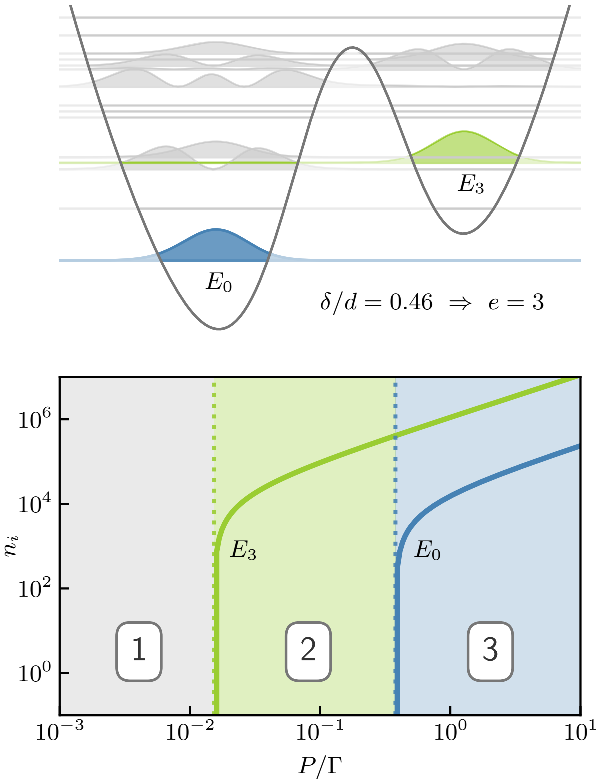

FIGURE 7.2: Lower panel: analytically obtained mode populations $n_{0,e}$ vs P for $\xi = 1$ and $\delta/d = 0.46$, for which the excited modes (E_3) is selected first, followed by the ground-mode selection. The two threshold values of P, indicated by dotted vertical lines, separate three regimes (pump-rate intervals), labeled 1, 2 and 3. They correspond to the three qualitatively different solutions of the system of equations (7.3). Upper panel: the double-well potential for this value of δ with the two selected modes shown in color.

used definition (3.17). One solution is $n_e = 0$, while setting the expression in the curly brackets to zero, gives the condition for a nonzero n_e. We get

$$G_e = \frac{R^e_\uparrow + \rho/\kappa}{R^e_\uparrow + R^e_\downarrow} = G_e^{th}, \tag{7.5}$$

which is, as expected, the already familiar condition for the threshold gain (3.25). Setting the first equation of the system (7.3) to zero, analogous condition is found for the gain of the ground mode $G_0 = f_1$.

From the last two equations it follows that in the regime where both modes are unselected, $n_0 = n_e = 0$, the fraction of excited molecules in the first bin is also zero, given that it is not pumped, while f_2 increases monotonically, $f_2 = P/(P + \Gamma)$. Inserting these results into the condition (7.5), we obtain the threshold pump rate of the excited mode e

$$P_e^{th} = \frac{G_e^{th}}{\alpha_2 - G_e^{th}} \Gamma. \tag{7.6}$$

When P is increased above this value, population of mode e becomes macroscopically large, while n_0 remains zero. Correspondingly, G_e is clamped (exactly) at G_e^{th}, while $G_0 = f_1$ starts to increase. For this second regime, n_e as a function of P is found using the last two equations of the system (7.3) together with the condition (7.5). Due to the length and complexity of the obtained expression, it is displayed in Appendix A.

Finally, above the second threshold P_e^{th} (regime 3), both of the modes become selected and the gain of both modes gets clamped, $G_0 = f_1 = G_0^{th}$ and $G_e = G_e^{th}$. The analytically obtained mode populations as functions of the pump rate, presented in Appendix A, are shown in Fig. 7.2 for a particular choice of parameters ξ and δ.

Figure 7.3 shows the mode populations as functions of P for 4 values of the parameter δ (roughly determining the double-well barrier position), while the thermalization parameter is held fixed at $\xi = 1$. We compare the analytically obtained $n_{0,e}(P)$ (dashed lines) with the numeric solutions (solid lines) of the full original rate equations [(3.15), (3.16)]. As always, the blue color corresponds to the ground mode, while the other colors represent the various excited modes e, which get selected at the respective value of δ. Given that the spontaneous emission is neglected in (7.3), the analytically obtained $n_{0,e}$ abruptly switch from zero to a large occupation at the thresholds (dotted lines). We can see that this simplified model very accurately predicts the two threshold pump rates, at least for these arbitrarily chosen values of δ and ξ. On the other hand, the macroscopic populations predicted by the model are quite larger than the numeric ones. This was to be expected, given that spontaneous emission is neglected and that only two modes are considered within the model.

We proceed to evaluate the agreement more systematically across a whole range of both

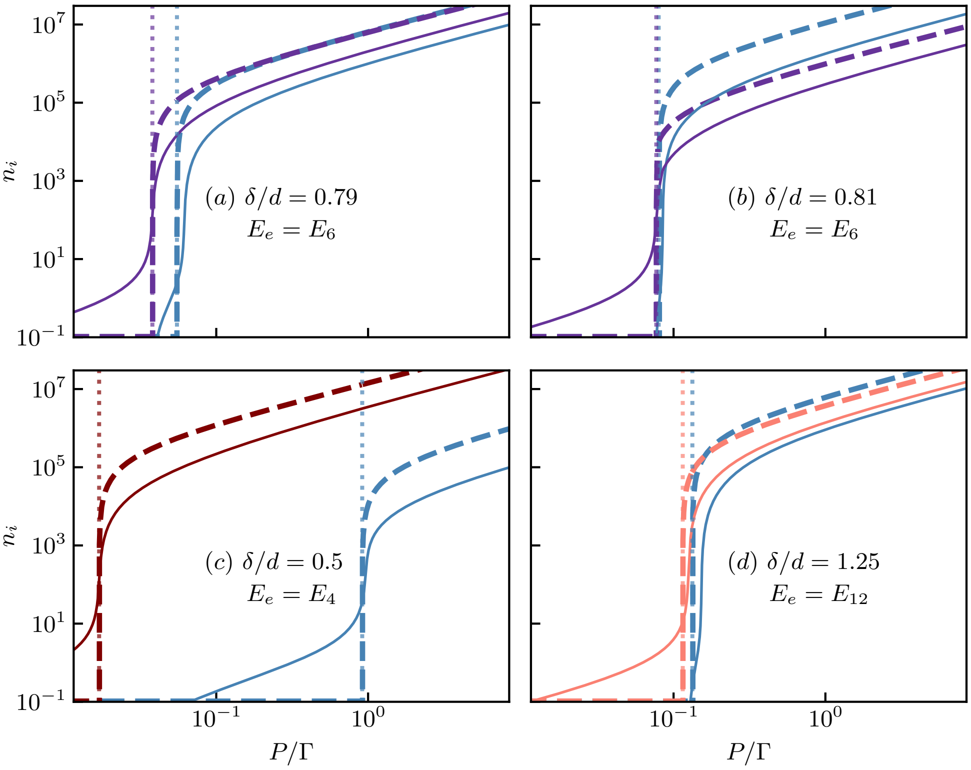

FIGURE 7.3: Mode populations $n_{0,e}$ vs P for $\xi = 1$ and 4 values of the parameter δ, for which various excited modes (E_e) shown in different colors are selected first, followed by the ground-mode selection (blue) in each case. Results obtained analytically using the simplified model are shown as dashed lines with the corresponding threshold P values marked by dotted vertical lines, whereas the numerical solutions of the original rate equations [(3.15), (3.16)] are shown as solid lines.

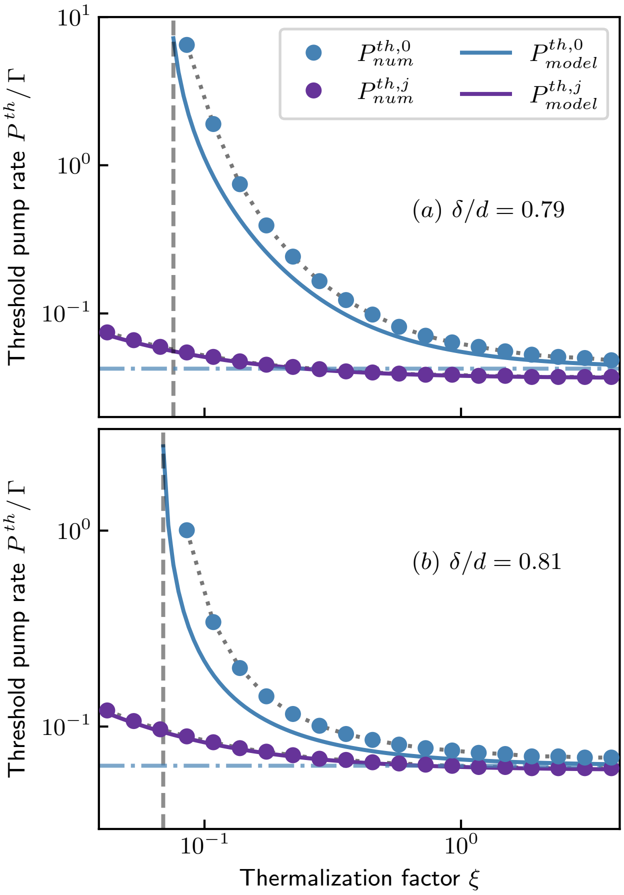

Figure 7.4: Threshold pump rate P^{th} vs ξ for the first selection of mode e (purple) and the second one of the ground mode (blue), for $\delta/d = 0.79$ (a) and $\delta/d = 0.81$ (b). The analytically obtained results (solid curves) are compared with the numerical ones (dots interpolated by dotted lines to guide the eye).

the thermalization factor and the δ parameter. In Fig. 7.4, we first show how the analytically obtained threshold pump rates $P^{th,0(e)}_{model}$ (solid lines) vary with the thermalization parameter, while δ is kept the same as in Fig. 7.3 (a, b), where the latter case (b) corresponds to an inter-well resonance. The numerical values $P^{th,0(e)}_{num}$ are indicated by dots. Unsurprisingly, the agreement for the first selection (purple) is excellent [1], while there are small deviations for the second threshold (blue). However, we can see that the agreement between the two solutions increases with ξ and they become barely distinguishable above $\xi \approx 1$. The blue curve asymptotes to the horizontal blue line, which indicates the minimum value of the second threshold [2]

$$P^{th,0}_{model}(\xi \to \infty) = \frac{\dfrac{R^0_{\downarrow}}{R^0_{\uparrow}} w_2 - \dfrac{R^e_{\downarrow}}{R^e_{\uparrow}} w_2 + \left(1 + \dfrac{R^e_{\downarrow}}{R^e_{\uparrow}}\right)(w_1 + w_2)\alpha_2}{w_2 \left[\dfrac{R^e_{\downarrow}}{R^e_{\uparrow}} + \dfrac{R^0_{\downarrow}}{R^0_{\uparrow}}\left(\alpha_2 + \dfrac{R^e_{\downarrow}}{R^e_{\uparrow}}\alpha_2 - 1\right)\right]}. \tag{7.7}$$

As expected from the discussion in the previous chapter, in the case of inter-well resonance, the first (purple) and second threshold (blue) become closer, due to the excited ("lasing") mode being approximately equally distributed between both wells. The vertical dashed line marks the lowest value of ξ for which the model predicts the occurrence of a ground-mode selection (below this value, $P^{th,0}_{model}$ becomes negative, and thus unphysical). This "cutoff" also matches the corresponding numerical one very well.

Finally, in Fig. 7.5, we compare how the analytic (solid lines) and the numeric threshold pump rates (dots) vary with δ, with $\xi = 1$. While the match for the first threshold (gray) is excellent across the whole range of δ, as expected, there are some deviations for the second one (blue), in particular between the resonances. The two lower panels show magnified regions around two of the resonance points (indicated by arrows in the top panel). We can see that the agreement is perfect for the first threshold, while the model consistently underestimates the P^{th} of the second threshold.

The very good agreement between the solutions of the simplified and the original rate equations in the double-well case suggests that this model should also be applicable to the case of the inhomogeneously pumped harmonic trap. The equations remain the same and the only difference is how the placement of the border between the two spatial regions is chosen. It is placed at a position between the ground mode and the pump, where they both become vanishingly small [3], as shown in Fig. 7.6. Again, the excited mode is distributed

---

[1] Given that the threshold P for the first transition can be obtained analytically even for the original rate equations, it is expected (and required) that the simplified model merely reproduces that result.

[2] Here, we explicitly write the expression for $P^{th,0}_{model}$ only in the limiting case $\xi \to \infty$. The general expression, given in Appendix A, is too long and complex to provide much insight.

[3] The same criterion is also automatically satisfied in the case of the double-well trap by placing the border at the center of the potential barrier.

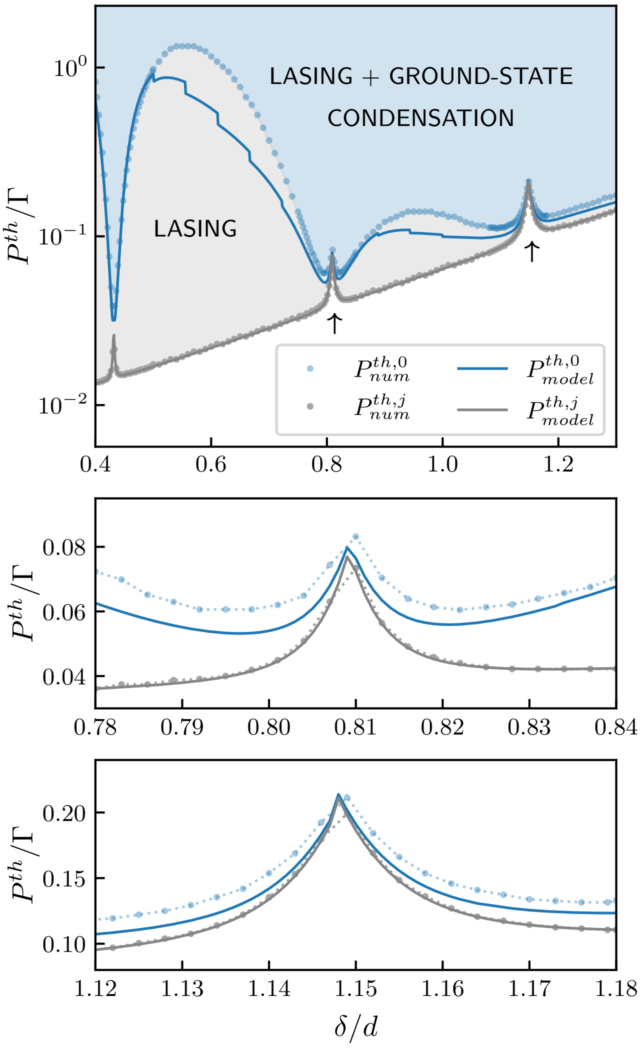

FIGURE 7.5: Top panel: threshold pump rate P^{th} vs δ for the first selection of the excited mode (gray) and the second one of the ground mode (blue). The analytically obtained results $P^{th,0(e)}_{model}$ (solid curves) are compared with the numerical ones, $P^{th,0(e)}_{num}$ (dots). The three qualitatively different regimes are shown with different colors, white (no modes selected), gray (only mode e selected) and blue (ground mode also selected). The two resonance points marked by arrows are shown magnified in the two lower panels.

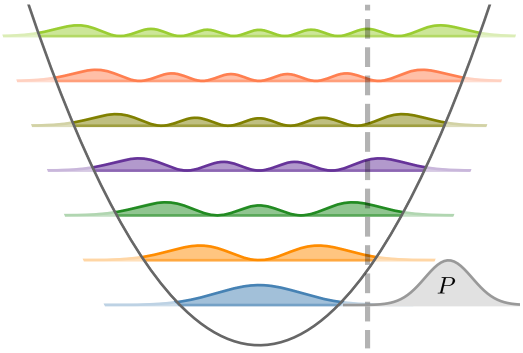

FIGURE 7.6: Simplified model applied to the case of asymmetrically pumped harmonic trap. The border between 2 spatial regions is placed between the ground mode and the pump, where they both become vanishingly small.

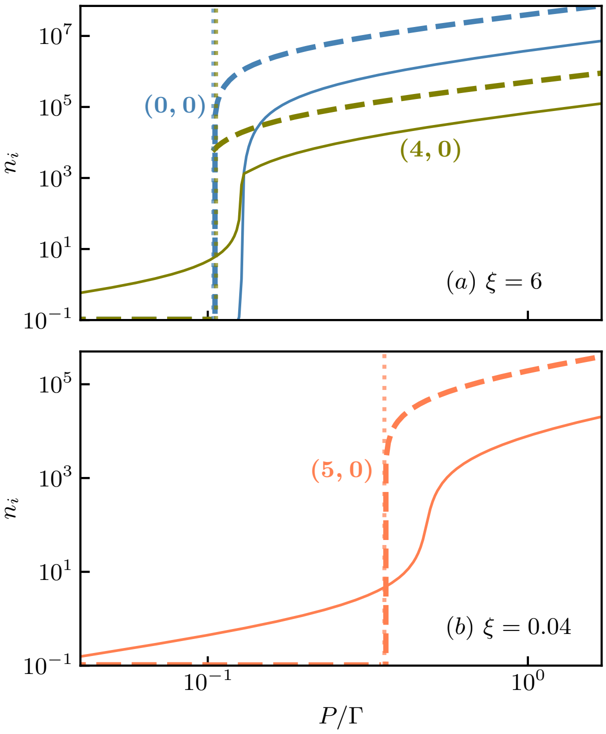

FIGURE 7.7: Mode populations $n_{(0,0)}$ and $n_{(e,0)}$ vs P for $\xi = 6$ (a) and $\xi = 0.04$ (b). Results obtained analytically using the simplified model are shown as dashed lines with the corresponding threshold P values marked by dotted vertical lines, whereas the numerical solutions of the original rate equations [(3.15), (3.16)] are shown as solid lines.

across both regions, while the ground mode is taken to be localized completely in the left region.

In Fig. 7.7 we show the mode populations as functions of P for 2 values of the thermalization parameter $\xi = 6$ (a) and $\xi = 0.04$ (b). These are the same values that were used in Chapter 5 where the numerical solutions of the original rate equations for the asymmetrically pumped harmonic trap are discussed. The agreement between the analytic (dashed) and the numeric solutions (solid lines) is still quite good, but the deviations are larger here, partly because the analytically solvable model requires a constant pump in the second bin, whereas a gaussian pump profile was used to obtain the numerical results. The model also accurately predicts that for the lower value of ξ [Fig. 7.7 (b)], the ground mode is not selected. This is indicated by the fact that the model produces a negative value of $P^{th,0}_{model}$ in this case.

This simplified model and the corresponding rate equations (7.3) can be easily modified to account for the case of a homogeneously pumped harmonic trap. Namely, a term $P(1-f_1)$ must be added to the third equation of (7.3), since both f_1 and f_2 are now pumped with a constant rate P. However, this model where the full spatial dependence is replaced with only two bins, is too crude to replicate the key effect of mode competition, i.e. the fact that, following the ground mode, the second mode to be selected at larger P is of successively higher energy as ξ increases. One of the reasons is that in the model, various excited modes are differentiated by their value of α_R, and not their overlap with the ground mode. While the latter decreases monotonically with the mode energy, the former does not. Another reason is that the detailed spatial dependence affecting how different modes overlap with each other, and correspondingly, the way in which the shape of $f(\vec{r})$ changes above threshold P, has an a an important role in the effect of mode competition. This means that it cannot be reproduced within a model which reduces $f(\vec{r})$ to only two values f_1 and f_2.

Chapter 8

Conclusions

We have studied how the variation of the photon cavity lifetime $1/\kappa$ and the cutoff frequency ω_c affects the steady state of a homogeneously pumped photon gas coupled to a dye medium. We have shown how, through the effect of mode competition (governed by the dye excitation profiles), the equilibrium-like ground-mode condensation emerges from the steady state of the system. Namely, we found that increasing the thermalization parameter $\xi \propto 1/\kappa$ produces a form of mode repulsion, in the sense that the ground-mode selection is followed by a selection of modes with increasing number of excitation quanta. This is explained as a consequence of how the dye excitation profile $f(\vec{r})$ at pump powers above which the ground-mode is selected, changes with ξ. We produced a phase diagram of the system in the space of 2 parameters, the pump power and the thermalization parameter and noted how it differs from the one in Ref. [31].

We then looked at the effect of varying cutoff frequency ω_c on the selection of modes, and found that, in agreement with previous work [10, 20, 24], below a certain value of ω_c, the photons are unable to effectively thermalize, resulting in the closely spaced selections of many excited modes, as opposed to the ground mode. On the other hand, the cutoff frequency can be increased above the value used in the rest of this work, while keeping the ratio of emission and absorption rates still to a good approximation proportional to the Boltzmann factor (i.e. the Kennard-Stepanov law still holds). We show that in this case only the ground mode is selected before the gain saturates.

We have also studied the case of an asymmetrically pumped photon gas, where a mechanism for controlled two-mode emission is observed. Namely, a transition to lasing in an excited cavity mode induced by an off-centered pump beam can trigger a second transition, where thermalization leads to the formation of a photon condensate in the ground mode. This mechanism can be made very robust and widely tuned by using a recently developed experimental technique for shaping the transverse potential for the photons in a trap. Namely, when pumping the upper minimum of an asymmetric double well, the second transition threshold can be shifted by orders of magnitude by tuning the system close to or further away from interwell resonances.

Finally, we formulated a simplified model which can be solved analytically and, for the case of asymmetrically pumped system, reproduces the qualitative features of the numerically obtained solutions of the full original model, while the quantitative agreement between the two models is also very good.

Appendix A

Full analytic solution of a simplified model

The population in the ground mode n_0 for the three regimes, as shown in Fig. A.1

$$n_0^1 = n_0^2 = 0,$$

$$\begin{aligned}
n_0^3 = {} & ((\tilde{R}^e_\uparrow + \tilde{R}^e_\downarrow)(-\tilde{R}^0_\downarrow + (\tilde{R}^e_\uparrow + \tilde{R}^e_\downarrow)\alpha_1)((1+p)w_2\alpha_1 - w_1\alpha_2) \\
& + \tilde{R}^0_\downarrow(-\tilde{R}^e_\uparrow(1+p)w_2\alpha_1(\tilde{R}^e_\uparrow - \tilde{R}^0_\downarrow + \tilde{R}^e_\downarrow + (\tilde{R}^e_\uparrow + \tilde{R}^e_\downarrow)\alpha_1) \\
& + (\tilde{R}^e_\uparrow + \tilde{R}^e_\downarrow)(\tilde{R}^e_\uparrow w_1 + (\tilde{R}^e_\uparrow + \tilde{R}^e_\downarrow)pw_2\alpha_1)\alpha_2 - \tilde{R}^e_\uparrow(\tilde{R}^e_\uparrow + \tilde{R}^e_\downarrow)w_1\alpha_2^2)\xi \\
& + \tilde{R}^e_\uparrow(\tilde{R}^0_\downarrow)^2 w_2\alpha_1(\tilde{R}^e_\uparrow(1+p) - (\tilde{R}^e_\uparrow + \tilde{R}^e_\downarrow)p\alpha_2)\xi^2 + (\tilde{R}^0_\uparrow)^2\xi(-\tilde{R}^e_\downarrow(1+p)w_2\alpha_1 \\
& + \tilde{R}^e_\uparrow w_1\alpha_2 + \tilde{R}^e_\downarrow w_1\alpha_2 + (\tilde{R}^e_\downarrow(1+p)w_2\alpha_1(\tilde{R}^e_\uparrow(-1+\alpha_1) + \tilde{R}^e_\downarrow\alpha_1) \\
& + (\tilde{R}^e_\uparrow + \tilde{R}^e_\downarrow)(\tilde{R}^e_\downarrow(-w_1 + pw_2)\alpha_1 + \tilde{R}^e_\uparrow(w_1 - w_1\alpha_1))\alpha_2 - \tilde{R}^e_\uparrow(\tilde{R}^e_\uparrow + \tilde{R}^e_\downarrow)w_1\alpha_2^2)\xi) \\
& + \tilde{R}^0_\uparrow((\tilde{R}^e_\uparrow + \tilde{R}^e_\downarrow)(-(1+p)w_2\alpha_1 + w_1\alpha_2) + ((1+p)w_2\alpha_1(-((R^e_{\uparrow)})^2 \\
& + \tilde{R}^e_\uparrow\tilde{R}^0_\downarrow - \tilde{R}^e_\uparrow\tilde{R}^e_\downarrow - \tilde{R}^0_\downarrow\tilde{R}^e_\downarrow + (\tilde{R}^e_\uparrow + \tilde{R}^e_\downarrow)(\tilde{R}^e_\uparrow + 2\tilde{R}^e_\downarrow)\alpha_1) + (\tilde{R}^e_\uparrow + \tilde{R}^e_\downarrow)((\tilde{R}^e_\uparrow + \tilde{R}^0_\downarrow)w_1 \\
& - (\tilde{R}^e_\uparrow + \tilde{R}^e_\downarrow)(2w_1 - pw_2)\alpha_1)\alpha_2 - \tilde{R}^e_\uparrow(\tilde{R}^e_\uparrow + \tilde{R}^e_\downarrow)w_1\alpha_2^2)\xi \\
& - \tilde{R}^0_\downarrow(\tilde{R}^e_\uparrow(1+p)w_2\alpha_1(-\tilde{R}^e_\uparrow\tilde{R}^e_\downarrow + (\tilde{R}^e_\uparrow + \tilde{R}^e_\downarrow)\alpha_1) - (\tilde{R}^e_\uparrow + \tilde{R}^e_\downarrow)(\tilde{R}^e_\uparrow w_1 + (-\tilde{R}^e_\uparrow + \tilde{R}^e_\downarrow)pw_2\alpha_1)\alpha_2 \\
& + \tilde{R}^e_\uparrow(\tilde{R}^e_\uparrow + \tilde{R}^e_\downarrow)w_1\alpha_2^2)\xi^2))/((\tilde{R}^0_\uparrow + \tilde{R}^0_\downarrow)(\tilde{R}^e_\uparrow + \tilde{R}^e_\downarrow)r\alpha_2((\tilde{R}^e_\uparrow + \tilde{R}^e_\downarrow)\alpha_1 \\
& + \tilde{R}^0_\downarrow(-1 + \tilde{R}^e_\uparrow(-1+\alpha_2)\xi) + \tilde{R}^0_\uparrow(-1 + \tilde{R}^e_\downarrow\alpha_1\xi + \tilde{R}^e_\uparrow(-1+\alpha_1+\alpha_2)\xi))).
\end{aligned}$$

Here we use the dimensionless quantities

$$\begin{aligned}
r &= R^0_\uparrow/\Gamma, \\
p &= P/\Gamma, \\
\tilde{R}^i_{\uparrow,\downarrow} &= R^i_{\uparrow,\downarrow}/R^0_\uparrow.
\end{aligned}$$

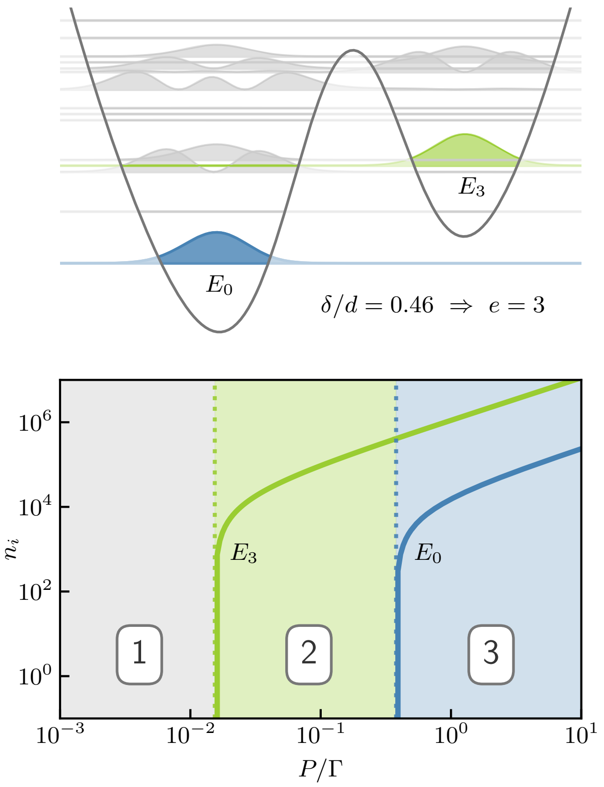

FIGURE A.1: Lower panel: analytically obtained mode populations $n_{0,e}$ vs P for $\xi = 1$ and $\delta/d = 0.46$, for which the excited modes (E_3) is selected first, followed by the ground-mode selection. The corresponding threshold values of P, indicated by dotted vertical lines, separate the three solutions of the system of equations (7.3). Upper panel: the double-well potential for this value of δ with the two selected modes shown in color.

The population in the excited mode n_e for the three regimes, as shown in Fig. A.1 is

$$n_e^1 = 0,$$

$$\begin{aligned} n_e^2 = {} & (-(\tilde{R}^e_\uparrow)^2(w_1(-1+\alpha_2)\alpha_2 + w_2\alpha_1(-1+\alpha_1+p(-1+\alpha_1+\alpha_2)))\xi \\ & + \tilde{R}^e_\downarrow(w_1\alpha_2 + w_2\alpha_1(1+p-\tilde{R}^e_\downarrow p\alpha_2\xi)) + \tilde{R}^e_\uparrow(w_2\alpha_1(1+p-\tilde{R}^e_\downarrow(-1+\alpha_1 \\ & + P(-1+\alpha_1+2\alpha_2))\xi) + w_1\alpha_2(1+\tilde{R}^e_\downarrow(\xi-\alpha_2\xi))) \\ & - ((\tilde{R}^e_\uparrow+\tilde{R}^e_\downarrow)^2(-4\tilde{R}^e_\uparrow w_2\alpha_1^2((1+p)w_2\alpha_1 - w_1\alpha_2)\xi(1+p+\tilde{R}^e_\uparrow\xi + p(\tilde{R}^e_\uparrow - (\tilde{R}^e_\uparrow+\tilde{R}^e_\downarrow)\alpha_2)\xi) \\ & + (w_1\alpha_2(-1+\tilde{R}^e_\uparrow(-1+\alpha_2)\xi) + w_2\alpha_1(1+p+(\tilde{R}^e_\uparrow(1+p)(1+\alpha_1) \\ & - (\tilde{R}^e_\uparrow+\tilde{R}^e_\downarrow)p\alpha_2)\xi))^2))^{1/2})/(2(\tilde{R}^e_\uparrow+\tilde{R}^e_\downarrow)^2 r\alpha_1\alpha_2(-1+\tilde{R}^e_\uparrow(-1+\alpha_1+\alpha_2)\xi)), \end{aligned}$$

$$\begin{aligned} n_e^3 = {} & (w_2((1+p)(\tilde{R}^0_\uparrow - \tilde{R}^e_\uparrow + \tilde{R}^0_\downarrow - \tilde{R}^e_\downarrow + \tilde{R}^e_\uparrow\tilde{R}^0_\downarrow\xi - \tilde{R}^0_\uparrow\tilde{R}^e_\downarrow\xi) \\ & + (\tilde{R}^e_\uparrow+\tilde{R}^e_\downarrow)(1+p+\tilde{R}^0_\uparrow\xi - \tilde{R}^0_\downarrow p\xi)\alpha_2))/((\tilde{R}^e_\uparrow+\tilde{R}^e_\downarrow)r\alpha_2(\tilde{R}^e_\uparrow - \tilde{R}^0_\downarrow + \tilde{R}^e_\downarrow \\ & - \tilde{R}^e_\uparrow\tilde{R}^0_\downarrow\xi + \tilde{R}^0_\uparrow(-1+\tilde{R}^e_\downarrow\xi) - (\tilde{R}^e_\uparrow + \tilde{R}^e_\downarrow - \tilde{R}^e_\uparrow\tilde{R}^0_\downarrow\xi + \tilde{R}^0_\uparrow\tilde{R}^e_\downarrow\xi)\alpha_2)). \end{aligned}$$

The threshold pump rate for the ground mode is calculated by setting $n_0^3 = n_0^2 = 0$ and solving it for P. The solution P_0^{th} is given by

$$\begin{aligned} P_0^{th} = {} & ((\tilde{R}^e_\uparrow + \tilde{R}^e_\downarrow - \tilde{R}^e_\uparrow\tilde{R}^0_\downarrow\xi + \tilde{R}^0\tilde{R}^e_\downarrow\xi)w_2(-1+\alpha_2)(\tilde{R}^0 - \tilde{R}^e_\uparrow + \tilde{R}^0_\downarrow - \tilde{R}^e_\downarrow + \tilde{R}^e_\uparrow\tilde{R}^0_\downarrow\xi \\ & - \tilde{R}^0\tilde{R}^e_\downarrow\xi + (\tilde{R}^e_\uparrow+\tilde{R}^e_\downarrow)(1+\tilde{R}^0\xi)\alpha_2) + (\tilde{R}^e_\uparrow+\tilde{R}^e_\downarrow)(1+\tilde{R}^0\xi)w_1\alpha_2(\tilde{R}^0 - \tilde{R}^e_\uparrow + \tilde{R}^0_\downarrow \\ & - \tilde{R}^e_\downarrow + \tilde{R}^e_\uparrow\tilde{R}^0_\downarrow\xi - \tilde{R}^0\tilde{R}^e_\downarrow\xi + (\tilde{R}^e_\uparrow + \tilde{R}^e_\downarrow - \tilde{R}^e_\uparrow\tilde{R}^0_\downarrow\xi + \tilde{R}^0\tilde{R}^e_\downarrow\xi)\alpha_2))/((\tilde{R}^e_\uparrow \\ & + \tilde{R}^e_\downarrow)(\tilde{R}^e_\uparrow + \tilde{R}^e_\downarrow - \tilde{R}^e_\uparrow\tilde{R}^0_\downarrow\xi + \tilde{R}^0\tilde{R}^e_\downarrow\xi)w_2(-1+\tilde{R}^0_\downarrow\xi + (\tilde{R}^e_\uparrow - \tilde{R}^0_\downarrow + \tilde{R}^e_\downarrow \\ & - \tilde{R}^e_\uparrow\tilde{R}^0_\downarrow\xi + \tilde{R}^0(-1+\tilde{R}^e_\downarrow\xi))/((\tilde{R}^e_\uparrow+\tilde{R}^e_\downarrow)\alpha_2))(-1+\alpha_2)\alpha_2). \end{aligned}$$

Bibliography

[1] M. H. Anderson, J. R. Ensher, M. R. Matthews, C. E. Wieman, and E. A. Cornell, "Observation of bose-einstein condensation in a dilute atomic vapor", Science **269**, 198–201 (1995).

[2] K. B. Davis, M.-O. Mewes, M. R. Andrews, N. J. van Druten, D. S. Durfee, D. Kurn, and W. Ketterle, "Bose-einstein condensation in a gas of sodium atoms", Physical review letters **75**, 3969 (1995).

[3] H. Deng, G. Weihs, C. Santori, J. Bloch, and Y. Yamamoto, "Condensation of semiconductor microcavity exciton polaritons", Science **298**, 199–202 (2002).

[4] J. Kasprzak, M. Richard, S. Kundermann, A. Baas, P. Jeambrun, J. M. J. Keeling, F. M. Marchetti, M. H. Szymanska, R. Andre, J. L. Staehli, V. Savona, P. B. Littlewood, B. Deveaud, and L. S. Dang, "Bose-Einstein condensation of exciton polaritons", Nature **443**, 409–414 (2006).

[5] T. Byrnes, N. Y. Kim, and Y. Yamamoto, "Exciton-polariton condensates", Nature Physics **10**, 803–813 (2014).

[6] R. Balili, V. Hartwell, D. Snoke, L. Pfeiffer, and K. West, "Bose-einstein condensation of microcavity polaritons in a trap", Science **316**, 1007–1010 (2007).

[7] J. D. Plumhof, T. Stöferle, L. Mai, U. Scherf, and R. F. Mahrt, "Room-temperature Bose-Einstein condensation of cavity exciton-polaritons in a polymer", Nature Materials **13**, 247–252 (2014).

[8] Y. Sun, P. Wen, Y. Yoon, G. Liu, M. Steger, L. N. Pfeiffer, K. West, D. W. Snoke, and K. A. Nelson, "Bose-einstein condensation of long-lifetime polaritons in thermal equilibrium", Phys. Rev. Lett. **118**, 016602 (2017).

[9] A. E Siegman, *Lasers* (University Science Books, Mill Valley, Calif., 1986).

[10] J. Klaers, F. Vewinger, and M. Weitz, "Thermalization of a two-dimensional photonic gas in a 'white wall' photon box", Nature Physics **6**, 512–515 (2010).

[11] J. Klaers, J. Schmitt, F. Vewinger, and M. Weitz, "Bose-Einstein condensation of photons in an optical microcavity", Nature **468**, 545–548 (2010).

[12] J. Marelic and R. A. Nyman, "Experimental evidence for inhomogeneous pumping and energy-dependent effects in photon Bose-Einstein condensation", Phys. Rev. A **91**, 033813 (2015).

[13] R. Weill, A. Bekker, B. Levit, and B. Fischer, "Bose-Einstein condensation of photons in an erbium-ytterbium co-doped fiber cavity", Nature Communications **10**, 747 (2019).

[14]R. Rajan, P. Ramesh Babu, and K. Senthilnathan, "Photon condensation: A new paradigm for Bose-Einstein condensation", Front. Phys. **11**, 110502 (2016).

[15]R. A. Nyman and B. T. Walker, "Bose-Einstein condensation of photons from the thermodynamic limit to small photon numbers", Journal of Modern Optics **65**, 754–766 (2018).

[16]B. T. Walker, L. C. Flatten, H. J. Hesten, F. Mintert, D. Hunger, A. A. P. Trichet, J. M. Smith, and R. A. Nyman, "Driven-dissipative non-equilibrium Bose-Einstein condensation of less than ten photons", Nature Physics **14**, 1173 (2018).

[17]J. Marelic, L. F. Zajiczek, H. J. Hesten, K. H. Leung, E. Y. X. Ong, F. Mintert, and R. A. Nyman, "Spatiotemporal coherence of non-equilibrium multimode photon condensates", New Journal of Physics **18**, 103012 (2016).

[18]J. Schmitt, T. Damm, D. Dung, F. Vewinger, J. Klaers, and M. Weitz, "Observation of grand-canonical number statistics in a photon bose-einstein condensate", Phys. Rev. Lett. **112**, 030401 (2014).

[19]J. Keeling and P. Kirton, "Spatial dynamics, thermalization, and gain clamping in a photon condensate", Phys. Rev. A **93**, 013829 (2016).

[20]P. Kirton and J. Keeling, "Thermalization and breakdown of thermalization in photon condensates", Phys. Rev. A **91**, 033826 (2015).

[21]B. T. Walker, H. J. Hesten, R. A. Nyman, and F. Mintert, "Collective excitation profiles and the dynamics of photonic condensates", Physical Review A **100**, 053828 (2019).

[22]B. T. Walker, H. J. Hesten, H. S. Dhar, R. A. Nyman, and F. Mintert, "Noncritical slowing down of photonic condensation", Physical review letters **123**, 203602 (2019).

[23]J. Schmitt, "Dynamics and correlations of a Bose-Einstein condensate of photons", J. Phys. B: At. Mol. Opt. Phys. **51**, 173001 (2018).

[24]J. Schmitt, T. Damm, D. Dung, F. Vewinger, J. Klaers, and M. Weitz, "Thermalization kinetics of light: From laser dynamics to equilibrium condensation of photons", Phys. Rev. A **92**, 011602(R) (2015).

[25]J. Schmitt, T. Damm, D. Dung, F. Vewinger, J. Klaers, and M. Weitz, "Bose-einstein condensation of photons versus lasing and hanbury brown-twiss measurements with a condensate of light", in Laser spectroscopy: xxii international conference on laser spectroscopy (icols2015) (World Scientific, 2017), pp. 85–96.

[26]H. A. M. Leymann, D Vorberg, T Lettau, C. Hopfmann, C Schneider, M Kamp, S. Höfling, R. Ketzmerick, J Wiersig, S. Reitzenstein, and A Eckardt, "Pump-power-driven mode switching in a microcavity device and its relation to bose-einstein condensation", Physical Review X **7**, 021045 (2017).

[27]D. Vorberg, R. Ketzmerick, and A. Eckardt, "Unified theory for excited-state, fragmented, and equilibriumlike bose condensation in pumped photonic many-body systems", Physical Review A **97**, 063621 (2018).

[28]M. Radonjić, W. Kopylov, A. Balaž, and A. Pelster, "Interplay of coherent and dissipative dynamics in condensates of light", New J. Phys. **20**, 055014 (2018).

[29]E. Stein, F. Vewinger, and A. Pelster, "Collective modes of a photon bose–einstein condensate with thermo-optic interaction", New Journal of Physics **21**, 103044 (2019).

[30] D. Dung, C. Kurtscheid, T. Damm, J. Schmitt, F. Vewinger, M. Weitz, and J., “Variable potentials for thermalized light and coupled condensates”, Nature Photonics **11**, 565–569 (2017).

[31] H. J. Hesten, R. A. Nyman, and F. Mintert, “Decondensation in nonequilibrium photonic condensates: when less is more”, Phys. Rev. Lett. **120**, 040601 (2018).

[32] M. Vlaho and A. Eckardt, “Nonequilibrium mode competition in a pumped dye-filled cavity”, Physical Review A **104**, 063709 (2021).

[33] M Vlaho, H. A. M. Leymann, D Vorberg, and A Eckardt, “Controlled two-mode emission from the interplay of driving and thermalization in a dye-filled photonic cavity”, Physical Review Research **1**, 033191 (2019).

[34] S. H. Strogatz, *Nonlinear dynamics and chaos with student solutions manual: with applications to physics, biology, chemistry, and engineering* (CRC press, 2018).

[35] C. Kittel, *Elementary statistical physics* (Courier Corporation, 2004).

[36] W. J. Mullin, “Bose-einstein condensation in a harmonic potential”, Journal of low temperature physics **106**, 615–641 (1997).

[37] A. Einstein, “Quantentheorie des einatomigen idealen gases. zweite abhandlung”, Albert Einstein: Akademie-Vorträge: Sitzungsberichte der Preußischen Akademie der Wissenschaften 1914–1932, 245–257 (2005).

[38] P. Wurfel, “The chemical potential of radiation”, Journal of Physics C: Solid State Physics **15**, 3967 (1982).

[39] D. McCumber, “Einstein relations connecting broadband emission and absorption spectra”, Physical Review **136**, A954 (1964).

[40] P. Moroshkin, L. Weller, A. Saß, J. Klaers, and M. Weitz, “Kennard-stepanov relation connecting absorption and emission spectra in an atomic gas”, Physical review letters **113**, 063002 (2014).

[41] J. R. Lakowicz, *Principles of fluorescence spectroscopy* (Springer science & business media, 2013).

[42] J. Klaers, J. Schmitt, T. Damm, F. Vewinger, and M. Weitz, “Statistical physics of bose-einstein-condensed light in a dye microcavity”, Physical review letters **108**, 160403 (2012).

[43] R. H. Brown and R. Q. Twiss, “Correlation between photons in two coherent beams of light”, Nature **177**, 27–29 (1956).

[44] P. Kirton and J. Keeling, “Nonequilibrium model of photon condensation”, Phys. Rev. Lett. **111**, 100404 (2013).

[45] A. Einstein, “Zur quantentheorie der strahlung”, Mittl. Phys. Gesell. Zurich **18**, 47–62 (1916).

[46] D. Vorberg, W. Wustmann, R. Ketzmerick, and A. Eckardt, “Generalized bose-einstein condensation into multiple states in driven-dissipative systems”, Phys. Rev. Lett. **111**, 240405 (2013).

[47] D. Vorberg, W. Wustmann, H. Schomerus, R. Ketzmerick, and A. Eckardt, “Nonequilibrium steady states of ideal bosonic and fermionic quantum gases”, Physical Review E **92**, 062119 (2015).

[48]J. Schmitt, T. Damm, D. Dung, F. Vewinger, J. Klaers, and M. Weitz, “Thermalization kinetics of light: from laser dynamics to equilibrium condensation of photons”, Physical Review A **92**, 011602 (2015).

[49]R. A. Nyman, *Absorption and fluorescence spectra of rhodamine 6g*, `https://doi.org/10.5281/zenodo.569817`, 2017.

[50]H. Sigurdsson, I. A. Shelykh, and T. C. H. Liew, “Switching waves in multilevel incoherently driven polariton condensates”, Physical Review B **92**, 195409 (2015).